

# Resolvent-based modelling of coherent structures in a turbulent jet flame using a passive flame approach

Mario Casel<sup>a</sup>, Kilian Oberleithner<sup>a</sup>, Feichi Zhang<sup>b</sup>, Thorsten Zirwes<sup>b,c</sup>, Henning Bockhorn<sup>b</sup>, Dimosthenis Trimis<sup>b</sup>, Thomas L. Kaiser<sup>a,\*</sup>

<sup>a</sup>Laboratory for Flow Instabilities and Dynamics, Institute of Fluid Dynamics and Technical Acoustics, Technische Universität Berlin, Müller-Breslau-Straße 8, Berlin 10623, Germany

<sup>b</sup>Engler-Bunte-Institute, Division of Combustion Technology, Karlsruhe Institute of Technology, Engler-Bunte-Ring 1, Karlsruhe 76131, Germany

<sup>c</sup>Steinbuch Centre for Computing (SCC), Karlsruhe Institute of Technology, Hermann-von-Helmholtz-Platz 1, Karlsruhe 76131, Germany

## ARTICLE INFO

## ABSTRACT

### Keywords:

Resolvent analysis  
Linear stability analysis  
Coherent structures  
Turbulent jet flame  
Flame dynamics

Motivated by the recent success in finding coherent structures in turbulent flows and describing their noise emission using the Resolvent Analysis (RA), the method is applied to a turbulent jet flame at  $Re = 15,000$  and a corresponding non-reacting flow to investigate their axisymmetric dynamics. The RA, which in this study assumes a passive flame and neglects compressibility effects, is based on the governing equations linearized around the temporal mean state. It is validated against Spectral Proper Orthogonal Decomposition (SPOD) obtained from time-resolved snapshots. Both the temporal mean state and the snapshots are obtained by Large Eddy Simulation (LES). The SPOD reveals that an axisymmetric, convective Kelvin–Helmholtz (KH) instability is the dominant hydrodynamic mechanism in the jet flame within a narrow frequency band and incorporates up to 40% of the turbulent kinetic energy. Results show that the RA is capable of reproducing the mode shapes seen in the SPOD. The RA furthermore allows to address the origin of these hydrodynamic structures: While the corresponding KH mode in a non-reacting turbulent jet flow is most sensitive to perturbations in the nozzle boundary layer, the same dominant mode in the turbulent Bunsen flame is most receptive to perturbations in the region between the nozzle edge and the annular pilot burner. The results suggest that the strong density gradients in this region initiate perturbations in the baroclinic torque, which are feeding the KH mode. Finally, a linear stability analysis proves that the high sensitivity of the KH structure is due to resonance with stable linear eigenmodes, which explains its high energy content. By applying the RA to a turbulent reacting flow, this study opens up a new pathway in analyzing the role of hydrodynamic structures in reacting flows.

## 1. Introduction

Modern gas turbines are operated in the lean flame regime, due to its beneficial attributes regarding nitric oxide emissions. At the same time, for technical reasons, reaching perfectly premixed fresh gas conditions is nearly impossible in a real engine. Unfortunately, both the lean flame regime and partially premixed fresh gases make the flame especially prone to combustion instabilities, i.e., fluctuations in heat release rate [1,2]. There are two distinctively different mechanisms leading to combustion instabilities, which both are highly unwanted effects. In the first case, the heat release rate fluctuations are most notably mono-frequent and occur due to a feedback mechanism between an acoustic mode of

the combustion chamber and the heat release rate fluctuations [3]. These instabilities are of thermoacoustic nature and may restrict the operation range of a gas turbine or, in extreme cases, result in a destruction of the combustion chamber.

The second mechanism causing combustion instabilities occurs due to turbulence. In this case, the combustion instabilities, just like the turbulence, are of broad band nature [4]. The heat release rate oscillations occur either due to fuel ratio inhomogeneities, which are caused by turbulent mixing processes, or due to a direct interaction between turbulence and the flame front. These broad band heat release rate fluctuations act as a source term in the acoustic field, leading to direct combustion noise [5], which is currently in the focus of both research and industry due to increasingly strict legal restrictions on noise pollution of aero-engines [6].

For thermoacoustic instabilities, it has been common knowledge for several decades that the interaction of the flame with hy-

\* Corresponding author.

E-mail address: [t.kaiser@tu-berlin.de](mailto:t.kaiser@tu-berlin.de) (T.L. Kaiser).

**Nomenclature***Latin*

|                    |                                 |
|--------------------|---------------------------------|
| $c$                | Progress variable               |
| $c_p$              | Isobaric specific heat capacity |
| $D$                | Main nozzle diameter            |
| $f$                | Frequency                       |
| $\mathbf{f}$       | Body force/forcing              |
| $\mathbf{I}$       | Identity tensor                 |
| $\mathbf{L, B, A}$ | Linear operators                |
| $\mathbf{M}$       | RA weighting matrix             |
| $Ma$               | Mach number                     |
| $N$                | Number of                       |
| $p$                | Pressure                        |
| $Pr$               | Prandtl number                  |
| $\mathbf{q}$       | State vector/response           |
| $\mathbf{Q}$       | Spectral data matrix            |
| $R$                | Specific gas constant           |
| $\mathbf{R}$       | Resolvent operator              |
| $Re$               | Reynolds number                 |
| $\hat{\mathbf{S}}$ | Cross-spectral density          |
| $Sc$               | Schmidt number                  |
| $St$               | Strouhal number                 |
| $t$                | Time                            |
| $T$                | Temperature                     |
| $\mathbf{u}$       | Velocity                        |
| $h$                | Heat release                    |
| $U$                | Bulk velocity                   |
| $\mathbf{W}$       | SPOD weighting matrix           |
| $Y$                | Mass fraction                   |

*Greek*

|           |                                  |
|-----------|----------------------------------|
| $\alpha$  | Cell size                        |
| $\eta$    | Thermal conductivity             |
| $\lambda$ | SPOD eigenvalue                  |
| $\Lambda$ | Structural sensitivity           |
| $\nu$     | Kinematic viscosity              |
| $\rho$    | Density                          |
| $\sigma$  | Optimal Gain                     |
| $\phi$    | Optimal forcing                  |
| $\Phi$    | Equivalence ratio                |
| $\psi$    | Optimal response                 |
| $\omega$  | Angular frequency/LSA eigenvalue |

*Subscripts*

|                        |                            |
|------------------------|----------------------------|
| $(\cdot)_{\text{DFT}}$ | Discrete Fourier Transform |
| $(\cdot)_{\text{eff}}$ | Effective                  |
| $(\cdot)_r$            | Radial                     |
| $(\cdot)_{\text{seg}}$ | Segment                    |
| $(\cdot)_x$            | Streamwise                 |
| $(\cdot)_{\text{th}}$  | Thermodynamic              |
| $(\cdot)_t$            | Turbulent                  |
| $(\cdot)_0$            | Unburnt                    |

*Superscripts*

|                      |                       |
|----------------------|-----------------------|
| $(\cdot)^{\dagger}$  | Adjoint               |
| $(\cdot)$            | Complex Amplitude     |
| $(\cdot)^{\text{H}}$ | Conjugate-transposed  |
| $(\cdot)$            | Periodic fluctuation  |
| $(\cdot)'$           | Remaining fluctuation |
| $(\cdot)$            | Temporal mean         |
| $(\cdot)^{\text{T}}$ | Transposed            |

*Glossary*

|    |                    |
|----|--------------------|
| BC | Boundary Condition |
|----|--------------------|

|      |  |
|------|--|
| CFD  | Computational Fluid Dynamics             |
| CFL  | Courant-Friedrichs-Lewy                  |
| EVP  | Eigenvalue Problem                       |
| FE   | Finite Element                           |
| FTF  | Flame Transfer Function                  |
| GEVP | Generalized Eigenvalue Problem           |
| KH   | Kelvin-Helmholtz                         |
| LES  | Large Eddy Simulation                    |
| LSA  | Linear Stability Analysis                |
| RA   | Resolvent Analysis                       |
| RHS  | Right Hand Side                          |
| RST  | Reynolds-Stress                          |
| SGS  | Subgrid Scale                            |
| SPOD | Spectral Proper Orthogonal Decomposition |
| TFC  | Turbulent Flame-speed Closure            |
| TKE  | Turbulent-Kinetic-Energy                 |

drodynamic perturbations is one of the main causes of heat release rate fluctuations. Only In recent years however, research has been successful in finding more and more coherence in form of wave packets in turbulent flows. One method, which has proven valuable in this context, is the RA which goes back to the early works of Trefethen et al. [7], Farrell and Ioannou [8] and Reddy and Henningson [9], Reddy et al. [10]. The RA is based on a linearization of the governing equations around a temporal mean state. By optimizing a predefined gain function, it identifies the spatial distribution of a periodic volume forcing resulting in the strongest response. This way, not only the dynamic structures occurring in the flow can be reproduced, but the method also, and this is its key benefit, provides insight into the generation mechanisms of the very same structures. In recent years, the RA deepened the understanding of turbulent cold flow configurations, such as Couette [11], pipe [12] and channel flows [13,14], flat-plate [15], Blasius [16] as well as turbulent boundary layers [17], a wake behind a NACA airfoil [18] and circular jets [19–21]. In these studies and others, at least some order was brought to apparently chaotic turbulence. If transferred successfully to turbulent reacting flows, the method could be used in the long run to understand and control flame dynamics and subsequent effects such as noise generation. This is underlined by recent studies, focusing on noise emission of turbulence based on RA, such as Jeun et al. [22] and Pickering et al. [23]. Recently, RA was firstly applied to a reacting flow [24], however, not in order to reproduce wave packets in turbulence, but to reproduce the dynamic response of the flow to harmonic acoustic perturbations.

The recent advancements, motivate the present study to apply the method of RA to analyze turbulence in a generic Bunsen flame, with the goal to enhance the understanding of the generation of coherent hydrodynamic structures in a reacting flow as well as their interaction with the flame front. The configuration was previously investigated experimentally [25] and by means of LES [26]. In order to validate our approach against previous studies, the RA is additionally applied to the same configuration at non-reacting conditions.

In the present study, the RA is based on LESs which provide the time averaged fields, serving as input to the linearized method. Furthermore, SPOD [27,28], which constitutes the ideal validation basis for RA response modes [29], is applied to extract the most energetic wave packets from LES snapshots. While SPOD was previously applied to non-reacting, subsonic, transonic and supersonic jet flows in order to recover the dominant flow dynamics [21,30], the investigation of a low-swirl jet flame by Shoji et al. [31] is so far, to the authors' best knowledge, the only application of SPOD to a reacting flow. In addition to the RA, the related method of Linear

Stability Analysis (LSA) will provide further insight in the generation process of the wave packets.

In this study, RA and LSA use a passive flame approach, previously known from thermoacoustics [32], and the assumption of incompressibility of the flow. This way, the method focuses on purely hydrodynamic structures and neglects acoustic waves and source terms in the linearized equations due to chemical reactions.

Only global heat release rate fluctuations contribute significantly to flame noise [5,33] as well as to most types of thermoacoustic oscillations. As a consequence, this study focuses on axisymmetric perturbations alone, since only they can contribute to global heat release rate fluctuations in a symmetric configuration.

The paper is structured as follows: Section 2 describes the setup and results of the LES. The SPOD approach as well as the results for both the non-reacting and reacting conditions are discussed in Section 3. Section 4.1 presents the linearized framework for both RA and LSA as well as an outline of the numerical setup. In Section 4.2, the results from the linear framework analyses are presented and compared to those empirically obtained by SPOD. Section 5 concludes the results.

## 2. Flow configuration and LES

The empirical (SPOD) and the deterministic (RA and LSA) methods rely on time-resolved snapshots and time averaged fields, respectively. To provide this data, fully compressible reacting LES computations are performed. In the following, specifics on the flow configuration setup as well as an outline of the LES framework are given. The LES of the configuration under investigation was previously validated against experimental measurements in [34]. Since the focus of this work is on the RA, only the case setup and the basics of the numerical LES framework are discussed here. For a thorough discussion of the LES strategy, the interested reader is kindly referred to Zhang et al. [34]. Further discussion of the LES applied to different configurations can be found in [26,35–37].

Figure 1a illustrates an instantaneous snapshot of the temperature,  $T$ , and reaction rate,  $h$ , and gives insights into the configuration setup. The burner consists of a central converging nozzle with an area ratio of nine which is connected to a straight tube of diameter  $D = 35$  mm and length  $4.3D$  which ends at the main burner exit at  $x = 0$ . An annularly arranged nozzle with an inner and outer diameter of  $1.17D$  and  $1.34D$ , respectively, is connected to the exit plane and provides the pilot flow.

Both the main and the co-axial pilot burner are operated with a premixed methane/air mixture at an equivalence ratio of  $\Phi = 0.9$ , an initial temperature of  $T_0 = 293$  K, and ambient pressure of  $p_0 = 101.325$  kPa. The Reynolds number is based on the diameter,  $D$ , of the primary nozzle, the bulk velocity,  $U$ , at the exit plane and the kinematic viscosity,  $\nu_0$ , of the fresh gas and is  $Re = 15,000$  resulting in a flame with a thermal load of 14.5 kW. The Mach number,  $Ma = 0.022$ , is based on the bulk velocity and ambient air.

The computations are performed with the open-source code OpenFOAM [38] which solves the fully compressible Favre-filtered conservation equations governing mass, momentum and enthalpy. The Smagorinsky model [39] is applied to account for Sub-grid Scale (SGS) Reynolds stresses, along with constant turbulent Schmidt and Prandtl numbers,  $Sc_t = Pr_t = 0.7$ , for the unresolved scalar and heat fluxes. Turbulence-chemistry interactions are governed by a Turbulent Flame-speed Closure (TFC) model (for details see, e.g., [34]) which solves an additional transport equation for the Favre-filtered reaction progress variable. Species mass fractions from 1D freely-propagating, unstrained premixed methane/air flames are computed in Cantera [40] along with the GRI-3.0 reaction mechanism [41]. These are projected onto the

progress variable  $c$ , leading to a chemistry look-up table with the mass fractions of species  $j$ , as functions of  $c$ , i.e.,  $Y_j = f(c)$ .

The computational grid covers the inflow section depicted in Fig. 1a and a downstream, cylindrical domain with  $80D$  extension in streamwise and radial direction. The grid is locally refined towards the burner walls and the shear layer of the jet, having the smallest grid resolution of 0.3 mm in the radial direction. The computational grid consists of 11.2 million hexahedral grid cells in total. Figure 2 provides an overview of the computational domain and grid used.

At the entrainment and outlet boundaries, gradients of the velocity  $\mathbf{u}$ , the temperature  $T$  and the progress variable  $c$  are set to zero. No-slip conditions are used for the velocity on the nozzle walls. A turbulence inflow generator [42] has been used to reproduce experimentally measured flow velocities within the burner nozzle. A partially non-reflecting boundary condition [43] has been applied to all inlets, outlets and openings. As the overall maximum Mach number in the simulation is below 0.03, the interaction of acoustic waves with the flow can be neglected. The time step is therefore set to  $2.5 \cdot 10^{-5}$  s, which ensures a maximum Courant-Friedrichs-Lewy (CFL) number of approx. 0.8.

The time-average and one snapshot of the streamwise velocity based on the LES of the Bunsen flame are illustrated in Fig. 1b and 1c, respectively. The mean flame position is approximated by a black, dashed contour line of the temporally averaged progress variable ( $\bar{c} = 0.5$ ). In addition to the LES computations of the reacting flow, results for an equivalent non-reacting configuration are obtained.

## 3. Spectral proper orthogonal decomposition

### 3.1. Outline of the spectral proper orthogonal decomposition

In the pre-processing of the SPOD, the time average is subtracted from the LES velocity snapshots, which are interpolated on an unstructured grid of  $M$  discrete points. Subsequently, they are averaged in azimuthal direction to restrict the analysis to axisymmetric perturbations. After splitting the azimuthally averaged snapshots into  $N_{seg}$  overlapping segments of length  $N_{DFT}$ , a temporal Fourier decomposition is performed on each of the  $N_{seg}$  segments. The resulting  $N_{seg}$  spectra are resorted into spectral data matrices,  $\widehat{\mathbf{Q}}_{St_k}(\mathbf{x}) = [\widehat{\mathbf{q}}_{St_k}^{(1)}(\mathbf{x}), \widehat{\mathbf{q}}_{St_k}^{(2)}(\mathbf{x}), \dots, \widehat{\mathbf{q}}_{St_k}^{(N_{seg})}(\mathbf{x})] \in \mathbb{C}^{3M \times N_{seg}}$ , for each discrete dimensionless Strouhal number,  $St_k = f_k D/U$ , where  $k = 1, 2, \dots, N_{DFT}/2$  and where  $\widehat{\mathbf{q}}_{St_k}^{(j)} = [\widehat{\mathbf{u}}_{x,St_k}^{T(j)}, \widehat{\mathbf{u}}_{r,St_k}^{T(j)}, \widehat{\mathbf{u}}_{t,St_k}^{T(j)}]^T \in \mathbb{C}^{3M}$  incorporates the Fourier transforms of the velocity components of each segment  $j = 1, 2, \dots, N_{seg}$ . An inner product of the data matrices,  $\widehat{\mathbf{Q}}_{St_k}(\mathbf{x})$ , yields an approximation of the weighted cross-spectral density,  $\widehat{\mathbf{S}}_{St_k}$ , based on Welch's method, such as

$$\widehat{\mathbf{S}}_{St_k} = \frac{1}{N_{seg} - 1} \widehat{\mathbf{Q}}_{St_k}^H \mathbf{W} \widehat{\mathbf{Q}}_{St_k}, \quad (1)$$

where  $(\cdot)^H$  and  $(\cdot)^T$  denote the conjugate and ordinary transposed, respectively. The diagonal weighting matrix is defined as

$$\mathbf{W} = \text{diag}([\mathbf{w}^T, \mathbf{w}^T, \mathbf{w}^T]^T) \in \mathbb{R}^{3M \times 3M}, \quad \mathbf{w} = [\bar{\rho}_i \alpha_i r_i]_{i=1,2,\dots,M} \in \mathbb{R}^M, \quad (2)$$

which accounts for the temporal mean density  $\bar{\rho}$ , the grid cell size weight  $\alpha$  and the radius  $r$ , due to the cylindrical coordinate system. Finally, an eigenvalue decomposition of the cross-spectral density yields pairwise SPOD modes. These are (eigenvalue, eigenvector)-solutions at discrete, dimensionless Strouhal numbers  $St_k$ , which are sorted according to the eigenvalue magnitude in descending order. The eigenvector yields the spatial structure which incorporates the amount of turbulent kinetic energy associated with the

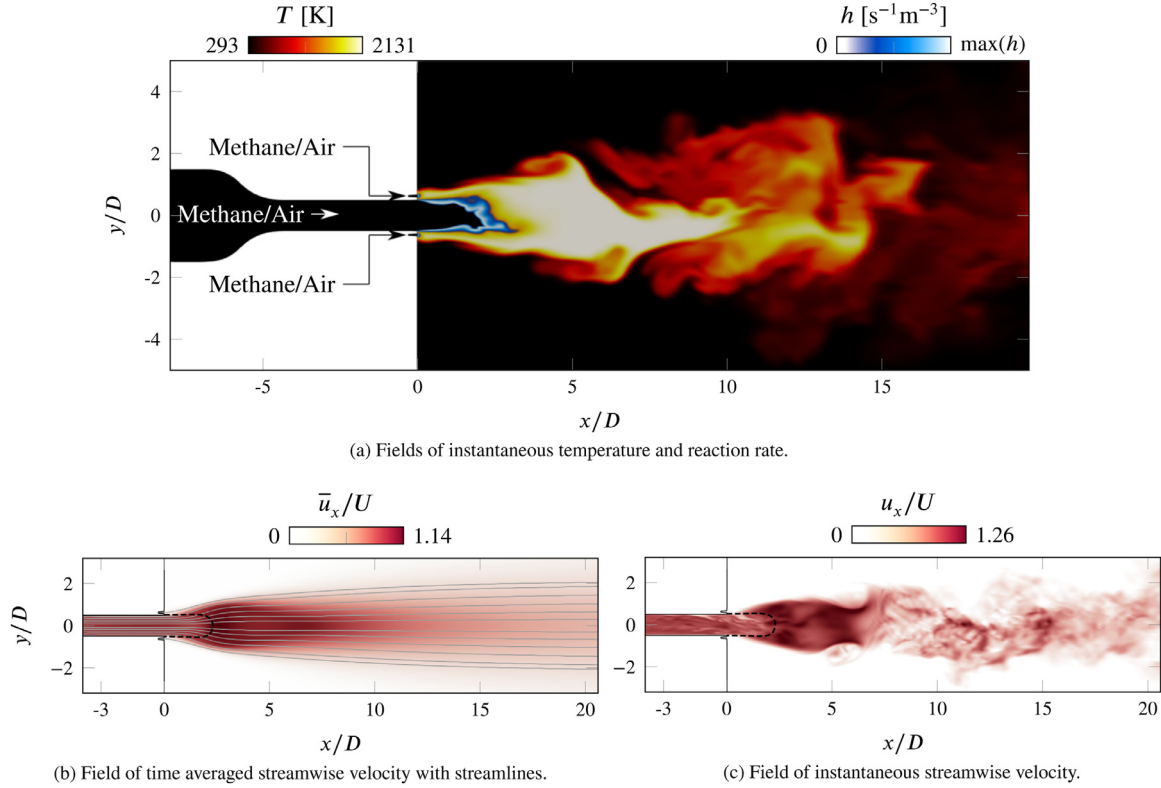


**Fig. 1.** Computational setup and flow fields of the turbulent Bunsen flame; The temporal mean flame position ( $\bar{c} = 0.5$ ) is displayed as black, dashed line.

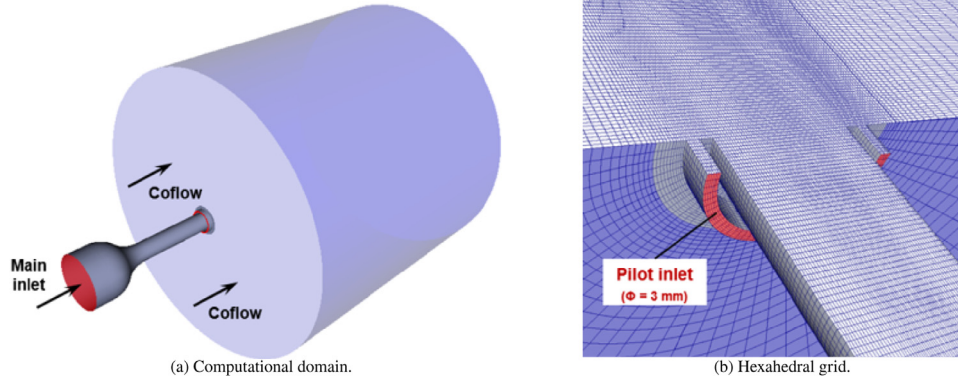


**Fig. 2.** Configuration for the LES.

eigenvalue. If one mode contains significantly more energy than all remaining modes and therefore dominates the flow in terms of energy, the flow is called to be of low-rank. The relative eigenvalue is introduced to measure the contribution of the  $i$ th mode on the total fluctuation energy of all  $N_{\text{seg}}$  modes at one particular Strouhal number  $St_k$ :

$$\lambda_i^*(St_k) = \frac{\lambda_i(St_k)}{\sum_{j=1}^{N_{\text{seg}}} \lambda_j(St_k)}, \quad i = 1, 2, \dots, N_{\text{seg}}. \quad (3)$$

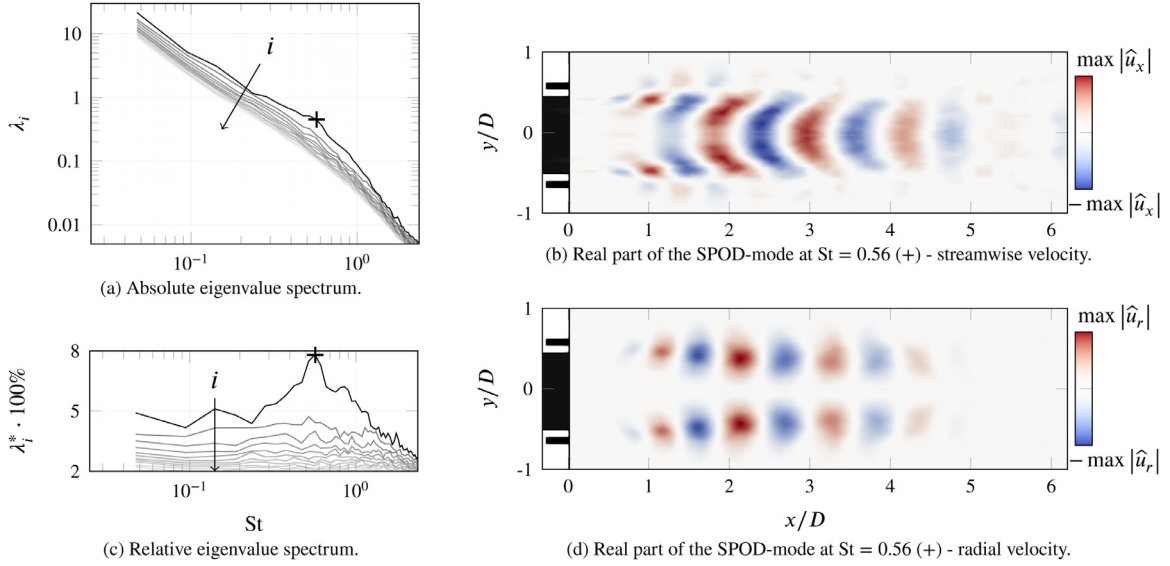
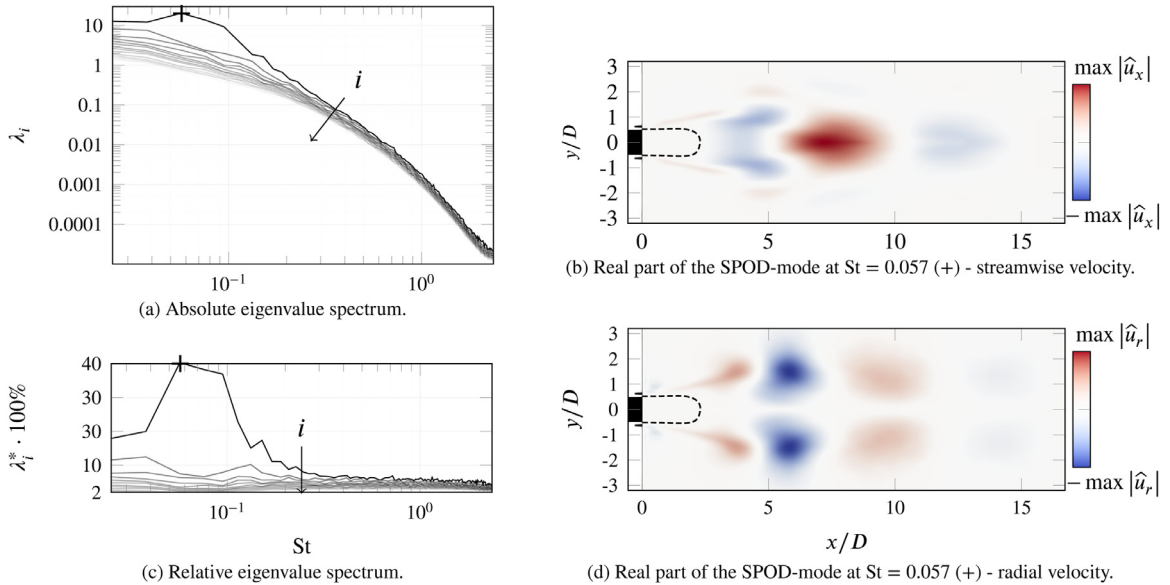
Eq. (3) is referred to as relative spectrum in the following.

Snapshots for both configurations are sampled with a rate of  $\Delta t = 1$  ms on a rectangular domain bounded by  $(x_{\min}, x_{\max}) = (0, 40)D$ . A total amount of 4800 snapshots is available for the non-reacting configuration and split into segments of length  $N_{\text{DFT}} = 100$  resulting in frequency resolution of  $St_0 = 0.0473$ . In case of the reacting flow, a higher number of 5600 snapshots is available allowing for a longer segment length of  $N_{\text{DFT}} = 250$  which results in a higher frequency resolution of  $St_0 = 0.0189$ .

### 3.2. Spectral proper orthogonal decomposition of the non-reacting configuration

Figure 3 illustrates eigenvalue spectra of the non-reacting configuration as a function of the dimensionless Strouhal number where the shading of the curves from black to white indicates the mode number in increasing order. The figure furthermore displays the streamwise and radial velocity components of the leading SPOD mode, exemplary for the frequency where it comprises most energy relatively.

Figure 3a shows that the magnitude of all eigenvalues monotonically decreases with frequency, while the leading eigenvalue displays a noticeable elevation from the remaining ones within the intermediate frequency range  $0.3 \lesssim St \lesssim 1.0$ . The relative spectra in Fig. 3c depicts that the leading mode incorporates up to 8% of the total turbulent kinetic energy at  $St = 0.56$ , while the second mode incorporates approximately 4% over the entire frequency range investigated. The SPOD spectrum therefore shows a clear mode separation.


**Fig. 3.** SPOD of the non-reacting configuration.

**Fig. 4.** SPOD of the reacting configuration.

ration between leading and remaining modes in the respective frequency range.

Figure 3b and 3 d shows the streamwise and radial components at the frequency of largest mode separation (see the +-marker in Fig. 3c). Both the streamwise and radial fluctuations originate and evolve in the potential core adjacent shear layer until they decay further downstream. Upstream of  $x \approx 1D$ , the spatial patterns of the streamwise velocity fluctuations are horizontally directed. Then, further downstream, they rotate into an orientation perpendicular to the streamwise direction. This vortex tilting is typical for KH-type wave packets which, together with the separation of the leading eigenvalue, has been identified as dominant within a similar frequency range in previous studies [21,30]).

### 3.3. Spectral proper orthogonal decomposition of the reacting configuration

Analogously to Figs. 3, 4 depicts the SPOD results of the reacting configuration.

While the absolute spectrum (Fig. 4a) displays a distinct elevation of the leading eigenvalue at low frequencies ( $0.04 \lesssim St \lesssim 0.15$ ), the relative spectra in Fig. 4c show that the leading SPOD mode incorporates up to 40% of the total fluctuation energy. This distinct mode separation is significantly stronger than in the non-reacting case and evidence for the low-rank behavior of the Bunsen flame at these frequencies. Moreover, the mode separation of the leading and the second mode occurs at far lower frequencies as well as within a much narrower frequency band. Corresponding to the maximum relative eigenvalue (see the +-marker in Fig. 4c), Figure 4b and 4 d shows the mode's streamwise and radial components, respectively. Similar to the non-reacting configuration, the mode shows a KH-type pattern, however with larger wavelength. Perturbations originate from the flame root and form horizontally directed patterns. In downstream direction, the wave packets spatially grow within the shear layer and are tilted similarly to the non reacting configuration (see Fig. 3b).

#### 4. Resolvent analysis and linear stability analysis

Unlike the purely empirical SPOD, linearized methods allow to describe the dynamics using a deterministic approach. In the following, the numerical strategy in the linearized framework is presented and subsequently, the results of both RA and LSA are discussed.

##### 4.1. Passive flame approach and linear framework methods

For the derivation of the linearized equations, additional simplifications are made in comparison with the LES in Section 2. These are:

1. The flow is considered in the low-Mach-number regime. This means that compressibility effects are neglected.
2. Following a similar approach known from thermoacoustics, heat release is modeled by a passive flame [32]. This means that fluctuations in density due to advective transport and turbulent heat diffusion are taken into account. Coherent fluctuations in the reaction chemistry and the therefrom resulting temperature and density fluctuations, on the other hand, are neglected.
3. Material properties are constant and equal for all species.
4. Source terms originating from chemical reactions, heat radiation, viscous heating are neglected.
5. The influence of product terms which include stochastic density fluctuations is neglected.

The non-linear conservation equations of mass, momentum and energy deduced from the above listed simplifications read

$$\frac{\partial \rho}{\partial t} + \nabla \cdot (\rho \mathbf{u}) = 0, \quad (4a)$$

$$\rho \left( \frac{\partial \mathbf{u}}{\partial t} + (\mathbf{u} \cdot \nabla) \mathbf{u} \right) = -\nabla p + \nabla \cdot \left( \frac{1}{\text{Re}} \left( (\nabla + \nabla^T) \mathbf{u} - \frac{2}{3} (\nabla \cdot \mathbf{u}) \mathbf{I} \right) \right) + \mathbf{f}_u, \quad (4b)$$

$$\frac{\partial \rho T}{\partial t} + \nabla \cdot (\mathbf{u} \rho T) = \nabla \cdot \left( \frac{1}{\text{Re Pr}} \nabla T \right), \quad (4c)$$

where  $\rho$ ,  $p$ , and  $\mathbf{f}_u$  denote the density, the dynamic pressure and an arbitrary body force, respectively.  $\mathbf{I}$  is the identity tensor. The Prandtl number is

$$\text{Pr} = \frac{\rho_0 \nu c_p}{\eta}, \quad (5)$$

where  $\rho_0$ ,  $c_p$  and  $\eta$  are the density of the unburnt mixture, the isobaric specific heat capacity and thermal conductivity, respectively. Note that the energy equation is formulated as a transport equation of temperature [44].

##### 4.1.1. Linearized equations

The triple decomposition introduced by Reynolds and Hussain [45] allows to address the problem of coherent fluctuations in the presence of stochastic turbulence. It decomposes the state variables into a temporally averaged, periodically fluctuating, and remaining fluctuating part which is decorrelated from the periodically fluctuating part. These contributions are indicated by  $(\bar{\cdot})$ ,  $(\tilde{\cdot})$  and  $(\cdot)'$ , respectively, and read

$$\begin{aligned} \mathbf{u} &= \bar{\mathbf{u}} + \tilde{\mathbf{u}} + \mathbf{u}', & p &= \bar{p} + \tilde{p} + p', & \rho &= \bar{\rho} + \tilde{\rho} + \rho', \\ \mathbf{f}_u &= \bar{\mathbf{f}}_u + \tilde{\mathbf{f}}_u + \mathbf{f}'_u, & T &= \bar{T} + \tilde{T} + T'. \end{aligned} \quad (6)$$

The periodic fluctuation is the difference between temporal and phase average. Substituting the triple decomposition into the non-linear governing equations (Eqs. (4)), neglecting terms of second

and higher order in periodic fluctuations and subtracting the temporal average of the resulting equations from its phase average yields

$$\frac{\partial \tilde{\rho}}{\partial t} + \nabla \cdot (\tilde{\rho} \tilde{\mathbf{u}}) + \nabla \cdot (\tilde{\mathbf{u}} \tilde{\rho}) = 0, \quad (7a)$$

$$\begin{aligned} & \tilde{\rho} \left( \frac{\partial \tilde{\mathbf{u}}}{\partial t} + (\tilde{\mathbf{u}} \cdot \nabla) \tilde{\mathbf{u}} + (\tilde{\mathbf{u}} \cdot \nabla) \tilde{\mathbf{u}} \right) + \tilde{\rho} \tilde{\mathbf{u}} \cdot \nabla \tilde{\mathbf{u}} \\ &= -\nabla \tilde{p} + \nabla \cdot \left( \text{Re}^{-1} \left( (\nabla + \nabla^T) \tilde{\mathbf{u}} - \frac{2}{3} (\nabla \cdot \tilde{\mathbf{u}}) \mathbf{I} \right) \right) \\ &+ \tilde{\mathbf{f}}_u - \tilde{\rho} \tilde{\mathbf{u}}' \cdot \nabla \tilde{\mathbf{u}}', \end{aligned} \quad (7b)$$

$$\tilde{\rho} \frac{\partial \tilde{T}}{\partial t} + \tilde{\rho} \tilde{\mathbf{u}} \nabla \tilde{T} + \tilde{\rho} \tilde{\mathbf{u}} \nabla \tilde{T} + \tilde{\rho} \tilde{\mathbf{u}} \nabla \tilde{T} = \nabla \cdot \left( \frac{1}{\text{Re Pr}} \nabla \tilde{T} \right) - \nabla \cdot (\tilde{\rho} \tilde{\mathbf{u}} \tilde{T}'). \quad (7c)$$

The linearized set of Eq. (7) was applied in previous studies for a local stability analysis [46] as well as global RA [24]. At this point, the system still is unclosed due the last term on the Right Hand Side (RHS) of both Eq. (7b) and (7c). Reynolds and Hussain [45] identify the first as the fluctuation of the background Reynolds-stresses due to the passage of periodic structures. In this study, they are modeled using an eddy-viscosity,  $\nu_t$  (see also [17,47–52]). Following Kaiser and Oberleithner [53], the remaining term on the RHS of Eq. (7c) is modeled analogously by using the gradient-diffusion hypothesis to relate it to an eddy-diffusivity,  $\eta_t$ .

After substituting both the eddy-viscosity and eddy-diffusivity models into Eq. (7) the harmonic ansatz

$$\tilde{\mathbf{q}} = [\tilde{\rho}, \tilde{\mathbf{u}}, \tilde{T}, \tilde{p}]^T = [\hat{\rho}, \hat{\mathbf{u}}, \hat{T}, \hat{p}]^T \exp(-i\omega t) = \hat{\mathbf{q}} \exp(-i\omega t), \quad (8a)$$

$$\tilde{\mathbf{f}} = [0, \tilde{\mathbf{f}}_u, 0, 0]^T = [0, \hat{\mathbf{f}}_u, 0, 0]^T \exp(-i\omega t) = \hat{\mathbf{f}} \exp(-i\omega t), \quad (8b)$$

is introduced for the variables of state, where  $\omega$  is a complex frequency, while  $(\hat{\cdot})$  and  $(\cdot)^T$  denote the complex amplitude of the respective state variable and the transposed, respectively. Similar to the empirically driven analysis by SPOD, only axisymmetric fluctuations are considered within the linearized framework which are governed by the ansatz in Eq. (8) (which neglects any azimuthal dependency). After substituting it into the system in Eq. (7), the resulting equations read

$$-i\omega \hat{\rho} + \nabla \cdot (\hat{\rho} \hat{\mathbf{u}}) + \nabla \cdot (\hat{\mathbf{u}} \hat{\rho}) = 0, \quad (9a)$$

$$\begin{aligned} & \hat{\rho} (-i\omega \hat{\mathbf{u}} + (\hat{\mathbf{u}} \cdot \nabla) \hat{\mathbf{u}} + (\hat{\mathbf{u}} \cdot \nabla) \hat{\mathbf{u}}) + \hat{\rho} \hat{\mathbf{u}} \cdot \nabla \hat{\mathbf{u}} \\ &= -\nabla \hat{p} + \nabla \cdot \left( \frac{1}{\text{Re}_{\text{eff}}} \left( (\nabla + \nabla^T) \hat{\mathbf{u}} - \frac{2}{3} (\nabla \cdot \hat{\mathbf{u}}) \mathbf{I} \right) \right) + \hat{\mathbf{f}}_u, \end{aligned} \quad (9b)$$

$$-i\omega \hat{\rho} \hat{T} + \hat{\rho} \hat{\mathbf{u}} \nabla \hat{T} + \hat{\rho} \hat{\mathbf{u}} \nabla \hat{T} + \hat{\rho} \hat{\mathbf{u}} \nabla \hat{T} = \nabla \cdot \left( \frac{1}{\text{Re}_{\text{eff}} \text{Pr}_{\text{eff}}} \nabla \hat{T} \right), \quad (9c)$$

where the effective Reynolds and Prandtl numbers read  $\text{Re}_{\text{eff}} = UD(\nu + \nu_t)^{-1}$  and  $\text{Pr}_{\text{eff}} = (\eta + \eta_t)[(\nu + \nu_t)\rho_0 c_p]^{-1}$ , respectively. The effective Prandtl number is fixed to  $\text{Pr}_{\text{eff}} = 0.7$ .

To finally close the set of equations, an eddy-viscosity model needs to be chosen. The choice is based on an evaluation by means of an alignment coefficient which compares the RA modes to those obtained by SPOD [54]. A comparison of different turbulence models has shown that the mixing length model, applied previously by Pickering et al. [30,47,55] performs best for the configuration and will therefore be used in this study.

In order to link both the mean and the coherent fluctuations of the temperature and density, respectively, the ideal gas law and its linearized counterpart are applied:

$$\bar{T} = \frac{p_{\text{th}}}{\bar{\rho} R}, \quad \hat{T} = -\frac{p_{\text{th}}}{R \bar{\rho}^2} \hat{\rho} = -\bar{T} \frac{\hat{\rho}}{\bar{\rho}}, \quad (10)$$

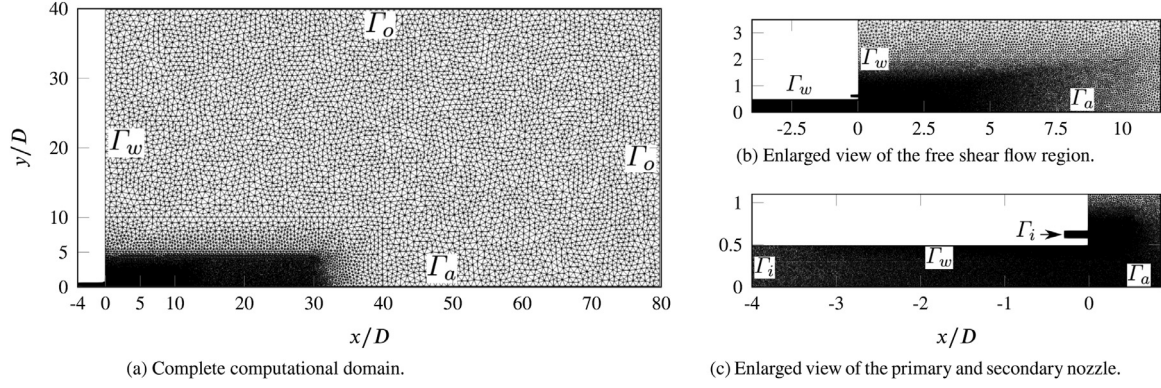


**Fig. 5.** Numerical domain and discretization for the linear framework;  $\Gamma_i$  are the boundaries, where a, i, o, w denote the inlet, the axis, the outlet, and the wall.

where  $R$  is the specific gas constant. Substituting these relations into Eq. (9) removes any dependency on the temperature and reduces the vectors for the state variables in Eq. (8) to  $\hat{\mathbf{q}} = [\hat{\rho}, \hat{\mathbf{u}}, \hat{p}]^T$  and  $\hat{\mathbf{f}} = [0, \hat{\mathbf{f}}_u, 0]^T$ . Due to the low-Mach-number assumption, the dynamic pressure,  $p$ , is decoupled from the thermodynamic pressure,  $p_{th}$  [56].

After spatially discretizing the resulting set of equations, it can be cast into the operator based notation

$$-\omega \mathbf{B} \hat{\mathbf{q}} + \mathbf{L} \hat{\mathbf{q}} = \hat{\mathbf{f}}, \quad (11)$$

where  $\mathbf{B}$  and  $\mathbf{L}$  denote the mean fields depending, discrete, operators, which in general are complex. In this study, analyses based on the whole set of Eq. (9) are referred to as low-Mach-number analyses, while the term cold-flow will refer to the simplified system without the linearized energy equation, where  $\bar{T} = \text{const.}$  and  $\hat{T} = 0$ .

#### 4.1.2. Linear stability analysis

In LSA, one considers the homogeneous problem leading to the Generalized Eigenvalue Problem (GEVP)

$$\omega \mathbf{B} \hat{\mathbf{q}} = \mathbf{L} \hat{\mathbf{q}}. \quad (12)$$

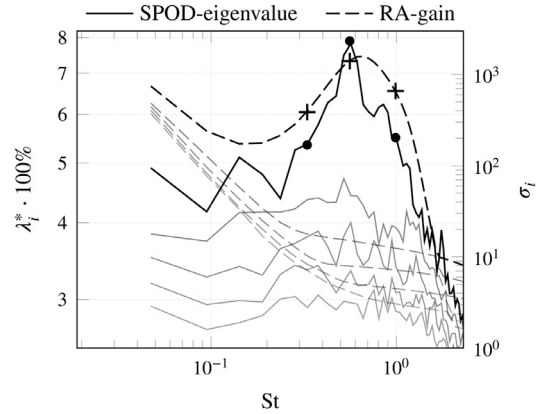
The real part of the eigenvalue,  $\omega_r$ , represents the angular frequency at which the mode oscillates in time. The imaginary part,  $\omega_i$ , is its temporal growth rate.

Solutions of the adjoint problem of Eq. (12) yield the adjoint eigenmodes. In this work, the adjoint problem is addressed by obtaining the complex conjugates of the discretized matrices,  $\mathbf{L}^\dagger$  and  $\mathbf{B}^\dagger$ , and subsequently solving the GEVP given by Eq. (12) for these adjoint operators. The adjoint eigenvectors describe which initial condition optimally excites their direct counterparts [57,58], and therefore reveal their receptivity to periodic perturbations.

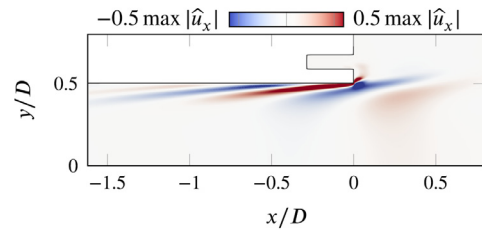
Given a pair of a direct and an adjoint mode, the internal feedback mechanism can be analyzed by determining the structural sensitivity,  $\Lambda(\mathbf{x})$ , which is defined as [59]

$$\Lambda(\mathbf{x}) = \frac{\|\hat{\mathbf{u}}^\dagger\| \cdot \|\hat{\mathbf{u}}\|}{\int \hat{\mathbf{u}}^\dagger \hat{\mathbf{u}} \, d\mathbf{x}}, \quad (13)$$

where  $(\cdot)^\dagger$  denotes adjoint. The structural sensitivity reveals the regions of strongest feedback of the global mode. It often is attributed to the wave maker region [59]. In this work, the norm in the nominator of Eq. (13) is the  $L_2$ -norm of all velocity components.



(a) Five leading, relative eigenvalues and five leading gains. The •- and + markers point to the mode shapes in Fig. 7.



(b) Streamwise component (real part) of the optimal forcing at  $St = 0.56$ .

**Fig. 6.** Comparison of SPOD and cold-flow RA of the non-reacting configuration and optimal forcing.

#### 4.1.3. Resolvent analysis

In contrast to the LSA, RA accounts for the harmonic body force in Eq. (11). The resulting, linear system is rearranged to

$$\hat{\mathbf{q}} = \underbrace{(\mathbf{L} - \omega \mathbf{B})^{-1}}_{=\mathbf{R}(\omega)} \hat{\mathbf{f}}, \quad (14)$$

where  $\hat{\mathbf{q}}$  and  $\hat{\mathbf{f}}$  are referred to as response and forcing in the context of RA. The operator  $\mathbf{R}$  is the resolvent operator, which linearly maps any arbitrary volume forcing,  $\hat{\mathbf{f}}(\omega)$ , onto the response. Note that in the context of RA  $\omega$  is the real-valued angular frequency and serves as an input parameter to the analysis.

In order to quantify the amplification between a response-forcing pair, a gain function,  $\sigma$ , is defined, which relates the in-

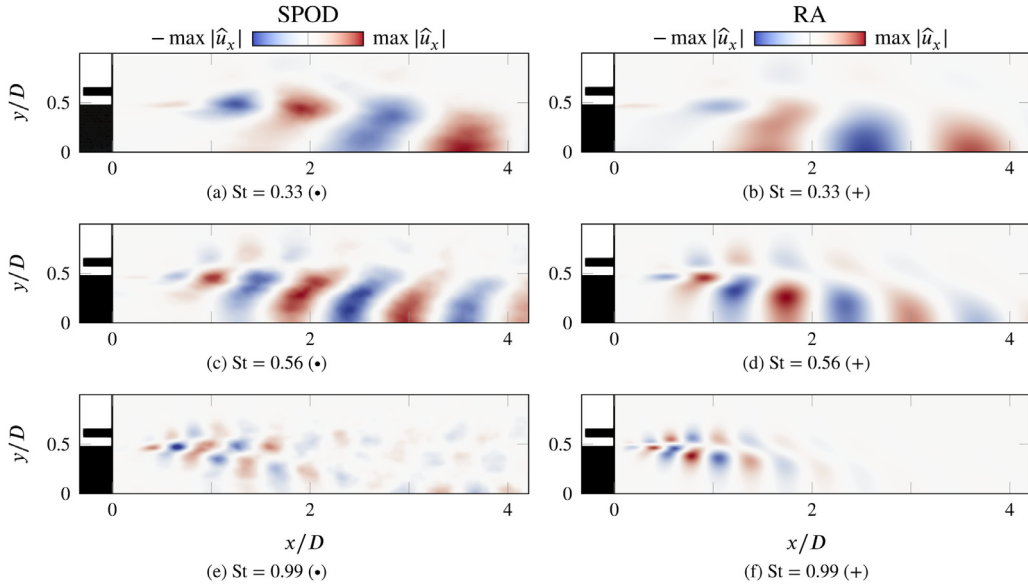


**Fig. 7.** SPOD modes (•, left column) and cold-flow RA responses (+, right column) of the non-reacting configuration (streamwise component, real part); Frequencies as indicated by the markers in Fig. 6a.

tegral energies of response and forcing

$$\sigma^2 = \frac{\hat{\mathbf{q}}^\dagger \mathbf{M}_q \hat{\mathbf{q}}}{\hat{\mathbf{f}}^\dagger \mathbf{M}_f \hat{\mathbf{f}}}, \quad (15)$$

where both  $\mathbf{M}_q$  and  $\mathbf{M}_f$  are the Finite Element (FE)-discretized inner products corresponding to

$$\langle \mathbf{v}, \mathbf{v} \rangle = \int \int \mathbf{v}^H \text{diag}(0, 1, 1, 1, 0) \mathbf{v} \bar{\rho} r dx dr, \quad (16)$$

for an arbitrary vector  $\mathbf{v}$  with the structure of  $\hat{\mathbf{q}}$  or  $\hat{\mathbf{f}}$ , respectively. In this study,  $\mathbf{M}_q$  and  $\mathbf{M}_f$  are identical and the index, therefore, will be dropped ( $\mathbf{M}_q = \mathbf{M}_f = \mathbf{M}$ ). The objective of RA is to find a frequency depending forcing-response pair that maximizes the gain. It can be shown [15] that this objective is addressed by solving the Eigenvalue Problem (EVP)

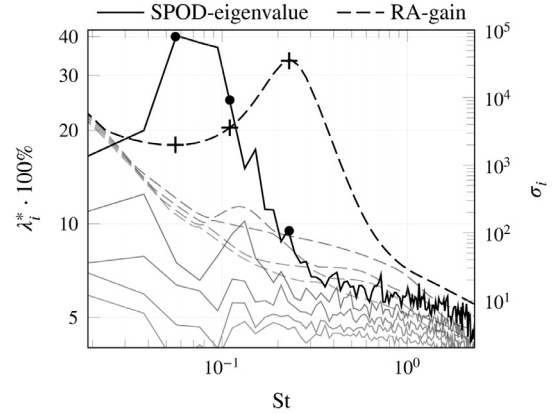
$$\mathbf{A} \hat{\phi} = \sigma^2 \hat{\phi}, \quad (17)$$

where  $\mathbf{A} = \mathbf{M}^{-1} \mathbf{R}^\dagger \mathbf{M} \mathbf{R}$ . The eigenvalues and eigenvectors of  $\mathbf{A}$  are the optimal, squared gains  $\sigma_i^2$  and optimal forcing modes  $\hat{\phi}_i$  which span an orthogonal basis of forcings. Applying the resolvent operator on the set of optimal forcings yields optimal response modes  $\hat{\psi}_i$  which also span an orthogonal basis. The resulting triplets of  $\{\hat{\phi}_i, \sigma_i, \hat{\psi}_i\}_i(\omega)$  are ranked according to the gain-magnitude in descending order. If the first, i.e., the leading, gain is significantly larger than the remaining ones, the resolvent operator is said to exhibit low-rank behavior at this particular frequency. In this case, the response to a forcing, which is not by coincidence close to orthogonal to the leading optimal forcing, can be approximated by the leading optimal gain, forcing and response alone.

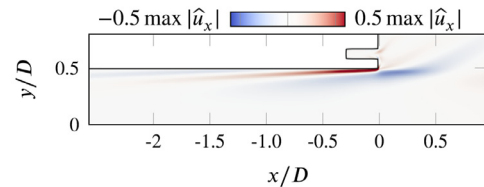
#### 4.1.4. Numerical approach for solving the linearized equations

The linear system in Eq. (11) is discretized and solved using the FELiCS solver. The solver uses a bi-global approach by taking advantage of the axisymmetry of the time averaged flow and solving the governing equations on a 2D grid. The domain is spatially discretized using the open source FE package fenics [60] with triangular continuous Galerkin elements of second order for the velocities and first order for the remaining quantities. To solve the linear systems given by Eqs. (12) and (17), the ARPACK library [61] is used.

Figure 5 provides the information on the spatial discretization and labels the boundaries. The Boundary Condition (BC) for axisymmetric perturbations [62] are applied at the axis. While homo-



(a) Five leading, relative eigenvalues and five leading RA gains. The •- and +- markers point to the mode shapes in Fig. 9.



(b) Streamwise component (real part) of the optimal forcing at  $St = 0.23$ .

**Fig. 8.** Comparison of SPOD and cold-flow RA of the reacting configuration and optimal forcing.

geneous Dirichlet conditions are applied for all fluctuation quantities at inlets and outlets, walls are treated with homogeneous Dirichlet conditions for the velocity and homogeneous Neumann conditions for pressure and density. The domain size in downstream direction was chosen as large as possible to avoid an interference between the periodic structures and unnatural outlet BCs [63].

Regions of high shear gradients, such as the shear layer as well as the boundary layer inside the nozzle are resolved with cell sizes down to  $1.7 \cdot 10^{-3} D$ , which is significantly smaller than the grid size in the LES. The resolution decreases in radial and streamwise

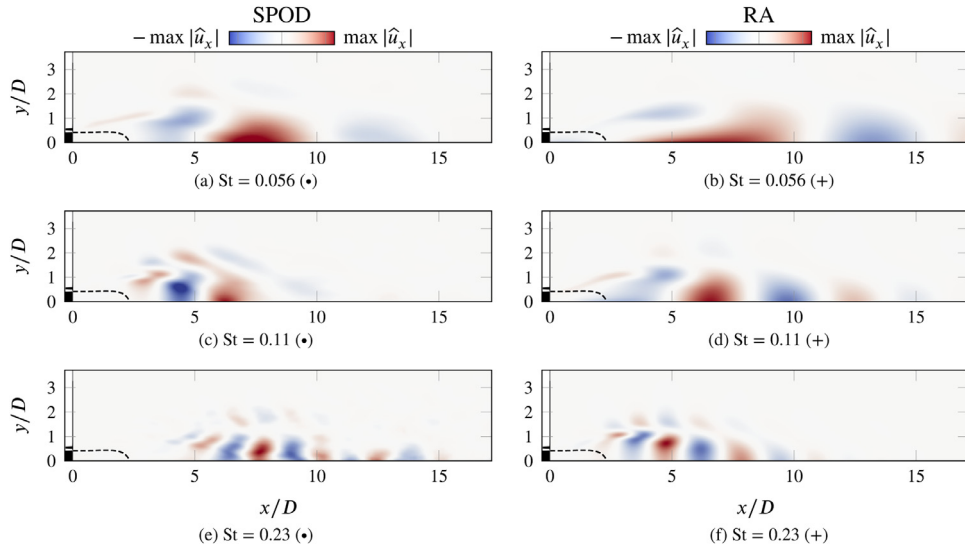


**Fig. 9.** SPOD modes ( $\bullet$ , left column) and cold-flow RA responses ( $+$ , right column) of the reacting configuration (streamwise component, real part); Frequencies as indicated by the markers in Fig. 8a.

directions downstream of the nozzle (largest cell size of approx.  $0.67D$ ). Mesh convergence studies for both the RA and the LSA confirm that a further refinement of the mesh presented in Fig. 5 has negligible influence on the results.

#### 4.2. Linear framework results

The linearized methods discussed in Section 4.1 are now applied to the mean flows obtained from LES. First, to validate our approach, the cold-flow analysis is applied to the non-reacting flow in Section 4.2.1. In order to examine the impact of the temperature change across the temporally averaged flame front and the resulting coherent temperature fluctuations, the linearized equations are applied using two different premises: First, the density change across the flame front is neglected by applying the cold-flow RA to the reacting mean flow in Section 4.2.2. Then the low-Mach-number equations, which take the inhomogeneous temperature field into account, are applied when performing RA and LSA of the reacting jet in Section 4.2.3 and 4.2.4, respectively.

##### 4.2.1. Cold-flow resolvent analysis of the non-reacting jet flow

The cold-flow RA is performed on the time average of the non-reacting flow. Figure 6a compares the spectra of the five leading RA gains to the five leading SPOD eigenvalues.

The spectra of the leading RA gain and the leading SPOD eigenvalue are in good agreement: Both the leading gains as well as the leading SPOD eigenvalues display a characteristic elevation approximately in the frequency range from  $St = 0.3$  to  $St = 1.2$ .

The streamwise component of the optimal forcing, which results in the maximum gain ( $St = 0.56$ ), is depicted in Fig. 6b. It is spatially confined within the nozzle boundary layer and displays a tilted and stratified structure with maximum amplitude at the nozzle exit. Such forcing patterns are observed across the entire frequency range where the resolvent operator exhibits low-rank behavior. These are known as Orr-type waves which were observed similarly in previous studies (e.g. by Garnaud et al. [19]), and constitute a typical evolution mechanism of KH wave packets in jet flows.

Optimal responses are obtained from projecting the optimal forcing (such as the one in Fig. 6b) onto the resolvent operator. Figure 7 compares their streamwise components to those of the leading SPOD modes at three frequencies (see the markers in

Fig. 6b). The wavelengths seen in the optimal responses and SPOD modes are in very good agreement. Minor discrepancies concern the different tilting angles of the structures especially for  $St = 0.33$  and  $St = 0.56$ , as well as the stronger streamwise decay of the optimal response seen for  $St = 0.56$ .

Overall, the agreement between the optimal responses and the SPOD modes is satisfactory and leads to the conclusion that the RA is capable of reproducing and explaining the origin of the KH-type structures observed in the LES of the non-reacting flow.

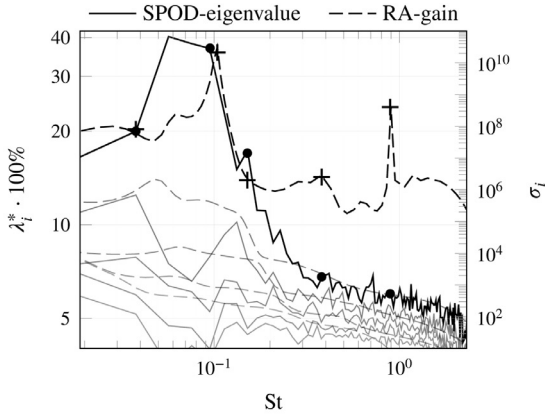
##### 4.2.2. Cold-flow resolvent analysis of the reacting configuration

Now, the cold-flow RA is applied to the reacting temporal mean flow, depicted in Fig. 1b. The resulting five leading gains from this analysis are compared to the five leading, relative SPOD eigenvalues in Fig. 8a.

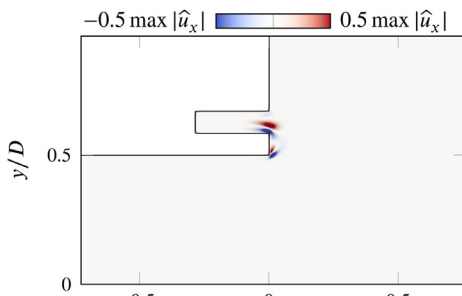
The resolvent operator exhibits a distinct low-rank behavior with a maximum of the leading gain at  $St = 0.23$ . In fact, the low-rank range shifts towards lower frequencies compared to the one identified in the leading gain of the non-reacting configuration. However, Figure 8a shows that it does not coincide with the low-rank range of the SPOD of the reacting configuration, which occurs at even lower frequencies. Moreover, the resolvent operator is of low-rank in a much broader frequency band than the SPOD (note the logarithmic frequency scale).

Figure 8b shows the streamwise component of the optimal forcing associated with the maximum gain at  $St = 0.23$  (Fig. 8a). The forcing is spatially confined within the boundary layer inside the nozzle and resembles the Orr-type forcing structures observed previously in the non-reacting configuration (Fig. 6b). Again, as in the non-reacting configuration, these spatial patterns are observed across the entire frequency range where the resolvent operator exhibits a low-rank behavior.

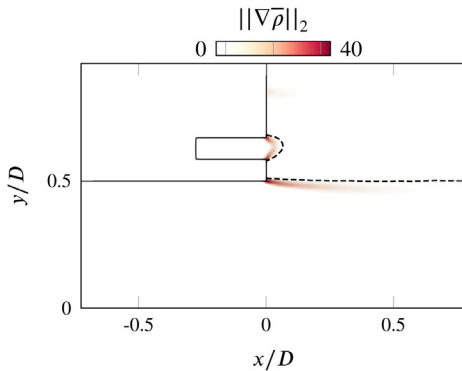
The streamwise components of the optimal response modes at the three frequencies marked in Fig. 8a are depicted in Fig. 9 and compared to the respective SPOD modes. For the highest frequency of  $St = 0.23$ , the optimal response and its SPOD counterpart show similar mode shapes. Nevertheless, the location of the maximum  $\hat{u}_x$ -fluctuation predicted by the RA is significantly further upstream ( $x \approx 5D$ ) than in the LES ( $x \approx 7.5D$ ). For lower frequencies, the RA appears not to capture the dynamics observed in the LES to a satisfactory degree: For the frequencies of  $St = 0.056$  and  $St = 0.11$ , the mode shapes of the RA and the SPOD expose significant differ-



(a) Five leading, relative eigenvalues and five leading RA gains. The  $\bullet$ - and  $\pm$ - markers point to the mode shapes in Fig. 11.



(b) Streamwise component (real part) of the optimal forcing at  $St = 0.1$ .



(c) Density gradient magnitude.

**Fig. 10.** Comparison of SPOD and low-Mach-number RA of the reacting configuration and optimal forcing.

ences, especially in regions upstream of  $x = 5D$ . This leads to the conclusion that the overall agreement between mode shapes is significantly worse than in the cold-flow configuration, at least if the temperature change across the flame front is ignored.

#### 4.2.3. Low-Mach-number resolvent analysis of the reacting configuration

In the previous paragraph, the density drop (or temperature increase) across the flame was neglected in the linearized framework. This violates both momentum and mass conservation, which could explain the discrepancies between SPOD and RA results. To correct this, the RA framework is extended to account for the density drop across the flame front due to the combustion heat using the low-Mach-number equations (Eq. (9)). As a consequence, the resolvent operator is formed using the inhomogeneous density field in addition to the temporal averages of the velocity (Fig. 1b).

Figure 10a compares the resulting five leading RA gain spectra to the five leading relative eigenvalues obtained by SPOD. The resolvent operator exhibits low-rank behavior over the entire frequency range. Within the lower frequency range ( $St < 0.2$ ), the leading RA gain exhibits a narrow peak which is in good agreement with the elevation of the leading eigenvalue observed in the SPOD spectrum.

The leading optimal forcing is exemplary shown in Fig. 10b for a frequency where both RA and SPOD exhibit a low-rank behavior ( $St = 0.1$ ). It distinctly differs from the Orr-type structures observed in the forcing of the non-reacting jet flow (Fig. 6b) as well as in the cold-flow RA neglecting non-uniform density (Fig. 8b): If the inhomogeneous density field is taken into account, the forcing is located at the edges of the primary nozzle and the pilot burner. This flow region coincides with the region of strongest temporally averaged density gradients, as can be seen in Fig. 10c. It appears that the inhomogeneity of the density field has a significant impact on the evolution mechanism of the wave packets. The mode itself, however, retains its KH-type wave pattern as can be seen in Fig. 11, which compares the leading optimal response to the modes identified empirically using SPOD. The figure demonstrates that taking into account the inhomogeneous density significantly increases the agreement of the leading optimal responses and SPOD modes in the frequency range, where the SPOD indicates low-rank behavior ( $St \lesssim 0.2$ ) in comparison to the cold-flow RA (see Figs. 8a and 9).

The dominant coherent structures are of KH type in both non-reacting and reacting configuration. However, evident differences in the optimal forcing of these configurations suggest different generation mechanisms. In fact, the optimal forcing in the reacting configuration is most significant in the flow region where maximum density gradients occur. This suggests that fluctuations in baroclinic torque could play an important role in the amplification process since they act as a source term in the transport equation of vorticity fluctuations [64].

While for low frequencies, leading optimal responses and SPOD modes agree well, the agreement deteriorates with increasing frequency (see Fig. 11). Small deviations are visible for  $St = 0.15$ , where wavelengths are overestimated for  $x < 10D$  in the RA response. Around this frequency, the low-rank characteristic of the SPOD diminishes showing no dominant coherent structures for  $St \gtrsim 0.2$ , while the low-Mach-number RA shows low-rank behaviour in the entire frequency range. Nevertheless, the RA gain in this frequency range is four orders of magnitude smaller compared to the global maximum at  $St = 0.1$ . Furthermore, the peak at  $St \approx 0.9$  is noticeable, but remains smaller by two orders of magnitude than the global maximum. While the SPOD mode shapes at this frequency do not show clear coherent structures (see Fig. 11g and 11i), the mode shapes of RA show wave patterns in the region of the flame tip (see Fig. 11h and 11j).

Besides the velocity modes, the low-Mach-number RA yields also modes describing the related density oscillation as a consequence to fluctuations in heat diffusion and advection. To compare these to the empirical density fluctuations in the LES, an additional SPOD is performed for the fields of density fluctuations. Figure 12 compares the density fields of the respective leading modes of RA and SPOD exemplary for  $St = 0.1$  showing good overall agreement. The SPOD mode demonstrates that the strongest coherent density fluctuations occur downstream of the flame. This shows that, at this frequency regime, the major part of density perturbations do not occur due to flame movement itself, but from an interaction of the coherent velocity fluctuations with the density gradients downstream of the flame front. The agreement between leading SPOD and RA modes deteriorates as the flow loses its low-rank characteristic with increasing frequencies, equivalently to the velocity modes seen in Fig. 11.

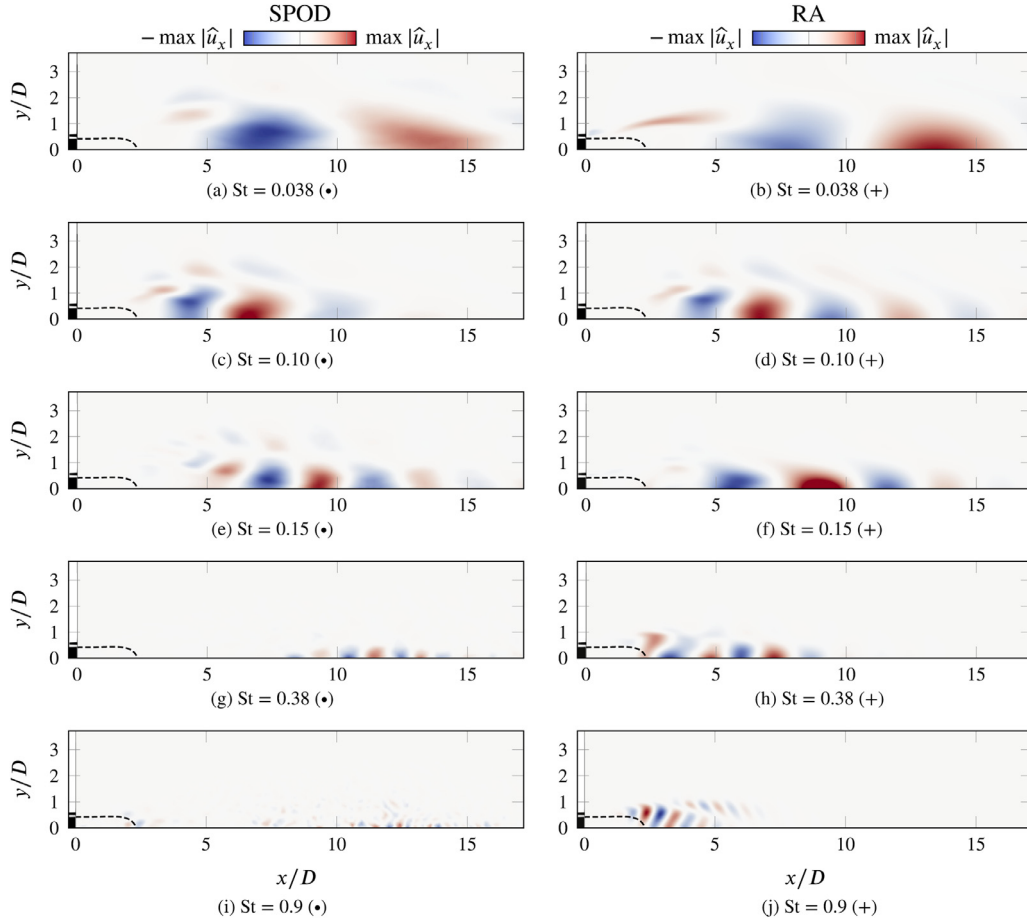


**Fig. 11.** SPOD modes (•, left column) and low-Mach-number RA responses (+, right column) of the reacting configuration (streamwise component, real part). Frequencies as indicated by the markers in Fig. 10a.

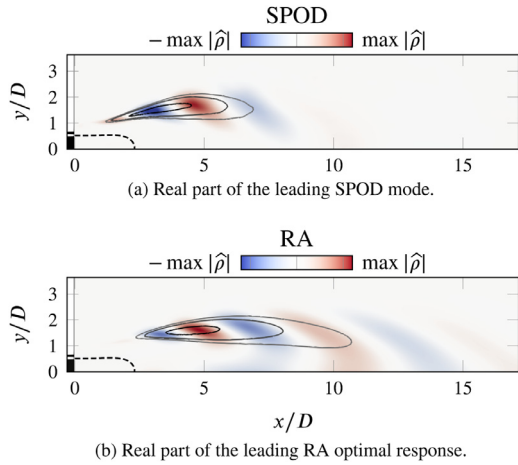


**Fig. 12.** Comparison of density fluctuations based on SPOD and RA at  $St = 0.1$ . Contour lines indicate 0.45, 0.60, 0.90 of the modulus' maximum.

In conclusion, the low-Mach-number RA using the passive flame approach appears to correctly describe the dynamics at low frequencies. For high frequencies however, the RA predicts a low-rank behavior of the flow, which is not seen in the SPOD results. As a consequence, the leading mode shapes of the RA and the SPOD agree for low frequencies, while they deviate for high frequencies. This is illustrated in Fig. 13, where an alignment factor [54], comparing the mode shapes of RA and SPOD, is plotted as a function

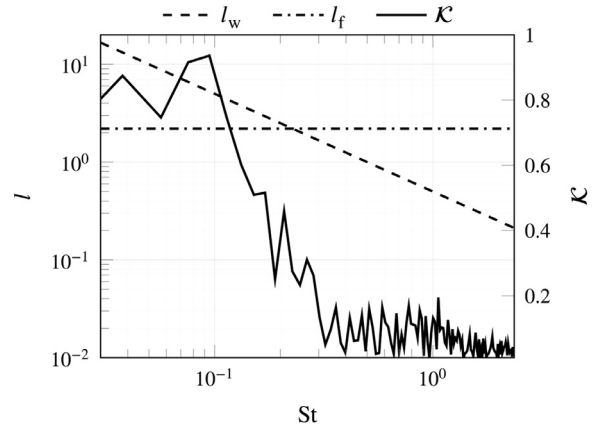


**Fig. 13.** Approximated wavelength  $l_w$  of the coherent structure, mean flame position at the jet center line  $l_f$  and alignment coefficient of the leading optimal solvent mode with the leading SPOD mode, based on Eq. (18), as a function of the Strouhal number; The wavelength is determined assuming a convection speed of half the flow centerline velocity at the exit plane of the nozzle,  $u_{x,cl}$ .

of the Strouhal number. The alignment factor is obtained by

$$\mathcal{K} = \frac{\langle \hat{\mathbf{u}}_x^{\text{SPOD}}, \hat{\mathbf{u}}_x^{\text{RA}} \rangle}{\|\hat{\mathbf{u}}_x^{\text{SPOD}}\|_2 \|\hat{\mathbf{u}}_x^{\text{RA}}\|_2}, \quad (18)$$

where  $\langle \cdot \rangle$  denotes the euclidian inner product and  $\|\cdot\|$  the associated norm.

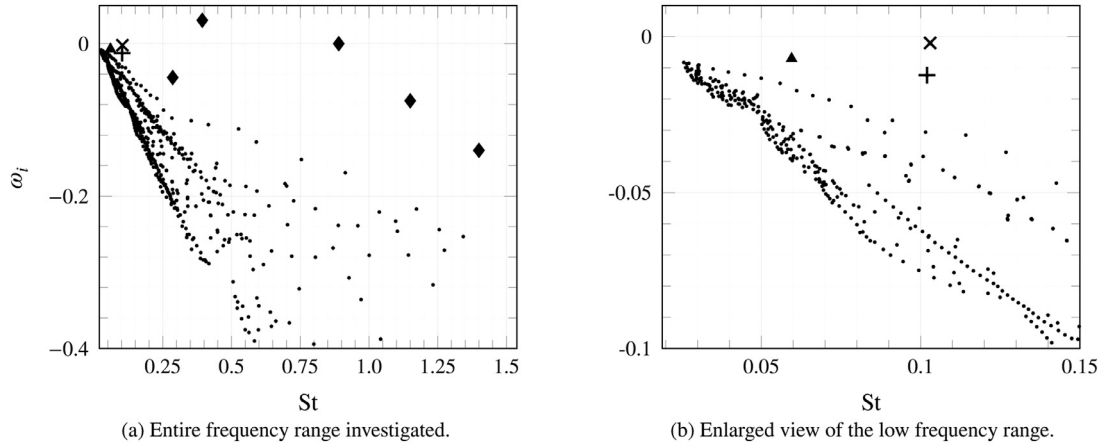


**Fig. 14.** Eigenvalue spectrum of the direct LSA of the reacting configuration; The  $\blacktriangle$ ,  $+$  and  $\times$  markers indicate the modes illustrated in Fig. 15.

A similar observation was made by Kaiser et al. [24], who analyzed the capability of the same low-Mach-number -RA/passive flame approach as used in this study to reconstruct the flame response to acoustic forcing. They found that for low frequencies the RA was capable of describing the flame response.

For higher frequencies, as in this study, their results differed from the empirical data. They supposed that the most decisive reason for this is the neglect of source terms in the linearized energy equation due to chemical reactions and the subsequent heat release of the flame. This explanation appears counter-intuitive, when considering studies focusing on the thermoacoustic behaviour of flames, which generally show that flames are predominantly active at low frequencies (see e.g. [65–68]). This general thermoacoustic property of flames manifests in the typical low pass behaviour of the FTF. However, at very low frequencies, where for premixed flames  $|\text{FTF}(\text{St} \rightarrow 0)| \rightarrow 1$ , the fluctuation in heat release is dominated by modulations of the flow rate into the combustion chamber and not by hydrodynamic waves, which become significant only with increasing frequency. This is shown for KH waves in [69] and for inertial/swirl waves in [70]. In the present configuration, which investigates these low frequencies, on the other hand, the flow is acoustically unperturbed and the wave patterns are of intrinsic origin. This means that no significant heat release oscillations are expected at very low frequencies (which is in agreement with studies focusing on flame noise, such as e.g. [34,71]). As a consequence, we uphold the presumption of [24], that the difference between the results of SPOD and RA at high frequencies is due to a lack of flame modelling in the RA.

To further analyze this claim, we assume that the deciding factor on how coherent wave packets interact with the flame front is their wavelength. Figure 13 compares the flame length with a simple approximation of the wave length of the perturbations, when assuming that they are advected at the half centerline speed of the fresh gases at the exit plane of the nozzle,  $u_{x,cl}$ . For low Strouhal numbers the wave lengths of the hydrodynamic perturbations are significantly larger than the flame (see also, e.g., Fig. 9c and 9d). While these structures lead to an advection of the entire flame, they are too large to fold the flame front and lead to flame wrinkles. As a consequence, they do not cause significant heat release fluctuations. This pure advection of the flame is taken into account in the passive flame approach. As the Strouhal number increases and the wave lengths are in the same order of magnitude as the flame length, they are able to wrinkle the flame front, which results in significant fluctuations in the reaction rate. This effect is not accounted for in the current passive flame approach, since it does not allow for fluctuations in chemical reactions and heat release. As a consequence the alignment in this frequency range de-

creases as illustrated in Fig. 13. To finally test this hypothesis it would be necessary to include the effect of coherent fluctuations in heat release in the resolvent framework in future studies.

#### 4.2.4. Linear stability analysis of the reacting jet flow

As seen in the previous section, a noticeable narrow peak occurs in the low-Mach-number RA gain spectrum which agrees well with SPOD results. Such elevations often occur due to intrinsic resonance with slightly damped global modes. In order to test this hypothesis, bi-global LSA based on the low-Mach-number equations (Eq. (9)) is applied to the time averaged flow (Fig. 1b).

Figure 14 depicts the eigenvalue spectrum obtained from the direct GEVP where the resulting growth rates,  $\omega_i$ , are depicted as a function of the Strouhal number. The spatial structures of the modes (not shown here) at  $\text{St} = 0.29, 0.39, 0.89, 1.19, 1.4$  ( $\blacklozenge$ -markers in Fig. 14) resemble the optimal RA responses at higher frequencies  $\text{St} \gtrsim 0.2$  (see Fig. 11h and 11 j). As shown in Section 4.2.3, the RA results do not agree with the SPOD results for higher frequencies ( $\text{St} \gtrsim 0.2$ ) which is assumed to be due to the lack of chemistry modeling linearized framework, which is a prerequisite to account for flame wrinkling. Therefore, the following analysis is restricted to the frequency range, where RA results are in good agreement with SPOD ( $\text{St} \lesssim 0.2$ ).

Three modes elevate from the remaining LSA eigenvalue spectrum ( $\blacktriangle$ :  $\text{St} = 0.059$ ,  $\times$ :  $\text{St} = 0.103$ , and  $+$ :  $\text{St} = 0.102$ , in Fig. 14). Figure 15 compares the streamwise velocity components of these global modes and the optimal RA responses at the respective frequencies, showing an excellent agreement for all three modes. Furthermore, the frequencies of the slightly damped modes are in very good agreement with noticeable elevations in the leading RA gain spectrum (Fig. 10a), including the dominant peak at  $\text{St} \approx 0.1$ , corresponding to the global mode with the lowest damping rate. Thus, the LSA results provide proof for the above raised hypothesis and indicate that an intrinsic feedback is the reason for the pronounced low-rank characteristic of the turbulent Bunsen flame and the related coherent velocity fluctuations observed in the LES.

In the following, the receptivity and intrinsic feedback of the least damped global mode ( $\text{St} = 0.103$ ,  $\times$  in Fig. 14) is studied in detail. Solving the adjoint GEVP yields the adjoint eigenmode of which the streamwise and radial velocity components are illustrated in Fig. 16b and 16 a, respectively. The illustration reveals the mode's most sensitive regions to periodic forcing, which are located between the primary and pilot burner nozzles. The streamwise component of the adjoint mode furthermore agrees well with the leading optimal RA forcing, depicted in Fig. 10b providing ad-

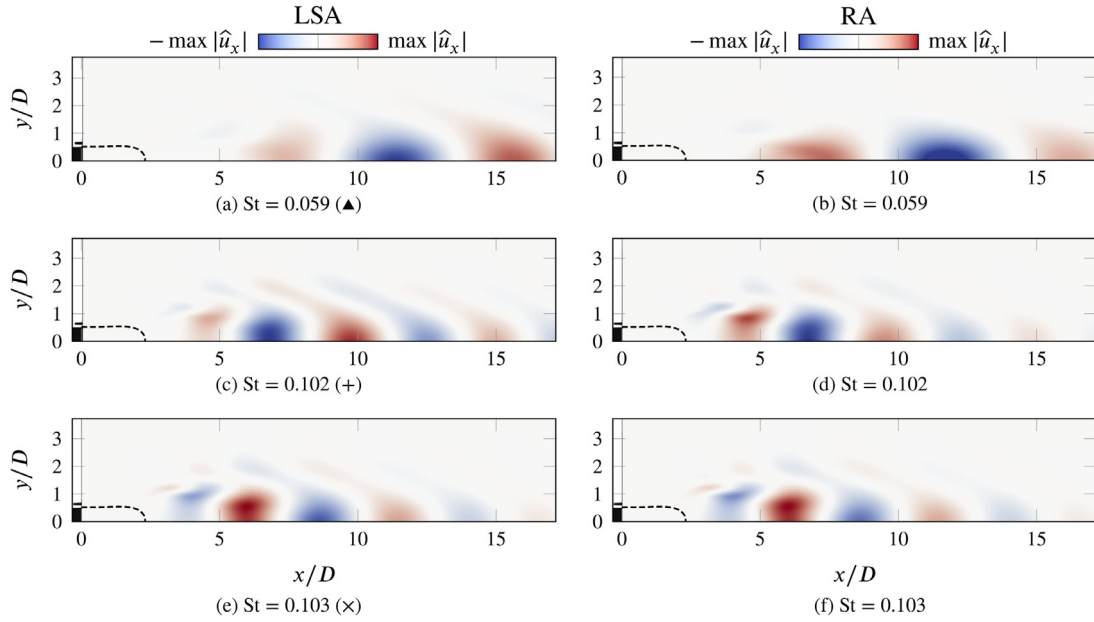


**Fig. 15.** Direct global modes and low-Mach-number RA of the reacting configuration (streamwise component, real part); Frequencies as indicated by the markers in Fig. 14.

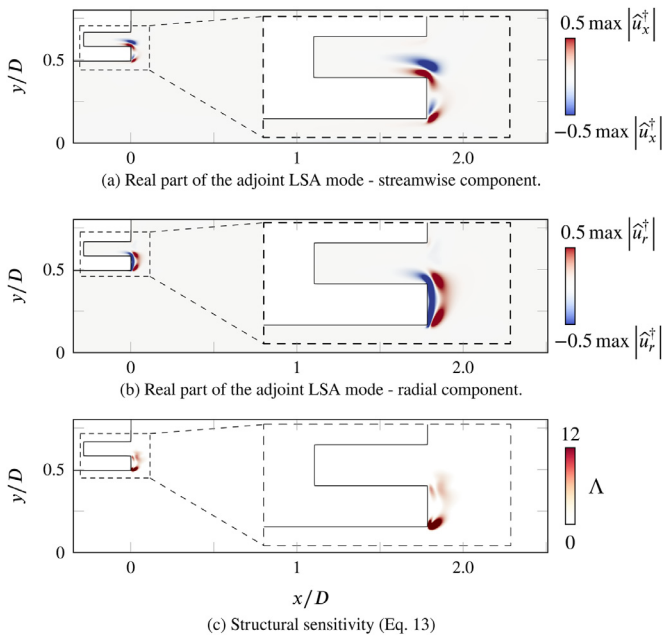


**Fig. 16.** Adjoint LSA modes and structural sensitivity associated with the direct mode at  $St = 0.103$  ( $\times$ ) in Fig. 14.

ditional evidence of the feedback causing the dominant flow structures seen in both RA and SPOD.

Finally, the structural sensitivity based on Eq. (13) is shown in Fig. 16c. The location of highest structural sensitivity reveals the region of strongest feedback which is located at the edge of the primary nozzle. These results emphasize the important role of the flow region between the primary and pilot burner nozzles for the global dynamics, at least at low frequencies. This information can be valuable for Computational Fluid Dynamics (CFD) or for attempts to reduce perturbations, for example via obstruction of the feedback, as shown by Kaiser et al. [72] or by modifying the mean flow in this region.

## 5. Conclusion

The present study investigates the axisymmetric dynamics of a turbulent jet flame ( $Re = 15,000$ ) using SPOD of time-resolved LES snapshots as well as the linear methods of RA and LSA.

The SPOD of velocity fluctuations in the turbulent Bunsen flame indicates low-rank behavior of the flow for a narrow frequency band, where the leading mode, which is of KH-type, incorporates up to 40% of the turbulent kinetic energy. It is shown that the low-rank characteristic of the flow is far more pronounced and the related mode significantly more dominant in comparison to the same flow configuration under non-reacting conditions.

Subsequently, a RA, which uses a passive flame approach in the low-Mach-number regime, is applied to the flow. For the frequency band in which the SPOD depicts low-rank behavior, both the spectra and mode shapes of SPOD and RA are in very good agreement. This indicates that the RA, when accounting for the inhomogeneous temperature field, captures the physical mechanisms which are relevant for the evolution of the coherent structures in this frequency range.

The RA furthermore proves that the mechanism leading to the KH mode differs significantly in reacting and non-reacting conditions. While under non-reacting conditions, the leading RA forcing shows Orr-type wave patterns in the boundary layer of the primary nozzle to be the origin of the KH wave packets, under reacting conditions, the KH mode is most efficiently forced in the region between the primary nozzle and the pilot burner. This location coincides with the regions of strongest density gradients, which indicates that baroclinic torque plays a significant role in the generation process of the KH structures.

For higher frequencies, the linearized approach appears not to capture the physics of the flow correctly, since here it predicts low-rank behavior and spatially coherent modes, and in doing so contradicts the SPOD results. It is assumed that this error at higher frequencies is due to the lack of chemistry modeling in the linearized framework.

Finally, a LSA explains the occurrence of the dominant coherent structures seen in both the SPOD and RA: The strong response to turbulent forcing within the narrow frequency band observed both in SPOD and the RA is due to harmonic resonance with slightly

damped global modes. Like the RA, the LSA attributes significant importance to the flow region between the primary nozzle and the pilot burners. Both the receptivity to periodic forcing as well as the intrinsic feedback is localized in this flow region. These results give indications for the control of the turbulent structures. Furthermore, care should be taken in CFD simulations to discretize this flow region well, in order to capture the therefrom developing flow structures correctly.

This study demonstrates the capability of the RA in combination with a passive flame approach to investigate the generation mechanism of coherent structures in a turbulent jet flame. The results furthermore show that the RA is a promising method for modeling combustion noise and thermoacoustics, once compressibility effects and fluctuations in chemistry are accounted for.

### Declaration of Competing Interest

The authors declare that they have no known competing financial interests or personal relationships that could have appeared to influence the work reported in this paper.

### Acknowledgements

The investigations were conducted as part of the joint research project “GREEN BELT – Dezentrale Gasturbinenanlagen für schnelle Reserven im Verbund mit erneuerbarer Energieumwandlung – Validierung der Technologien”. The work was supported by the German Federal Ministry for Economic Affairs and Energy (BMWi) under grant number 0324314B. The authors gratefully acknowledge MAN Energy Solutions SE for their support and permission to publish this paper. Funded by the Deutsche Forschungsgemeinschaft (DFG, German Research Foundation) Project-ID 441269395.

### Appendix A. Eddy-viscosity closure approach comparison

This section investigates different eddy viscosity models for the closure of the linear system in Eq. (9).

The first closing approach (called  $\nu^{\text{mol}}$ ), assumes  $\nu_t = 0$ . The second approach (Reynolds-Stress (RST)-model) relates the Reynolds stress and mean strain rate in the  $x - r$ -plane [73]

$$\nu_t^{\text{RST}} = \frac{-\overline{u'_x u'_r}}{\partial_r \overline{u_x} + \epsilon}, \quad (\text{A.1})$$

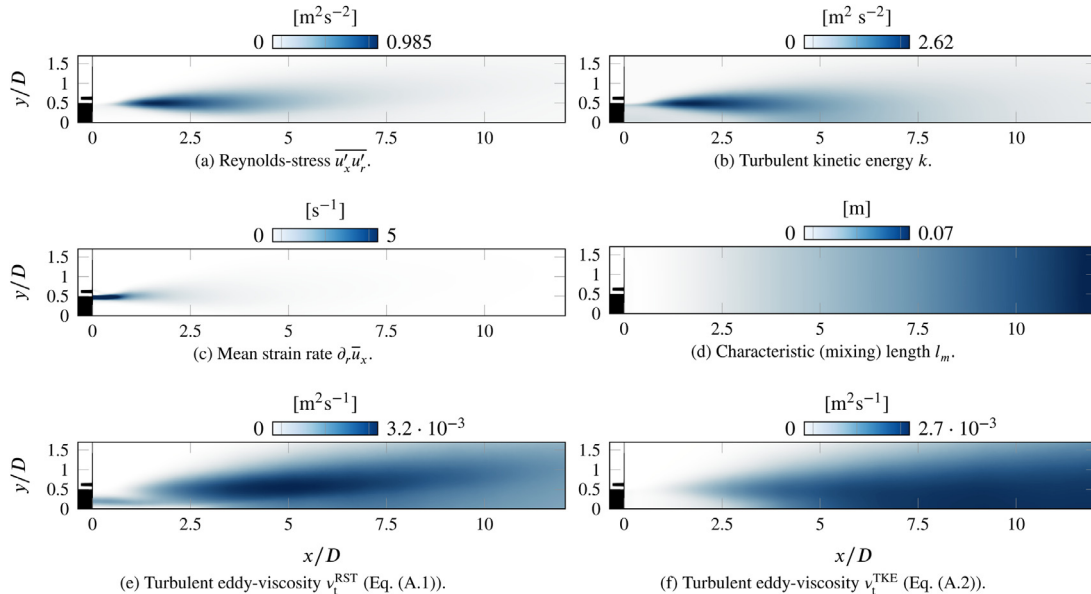


Fig. A.17. Turbulence characteristic quantities and eddy-viscosity of the RST and TKE-model.

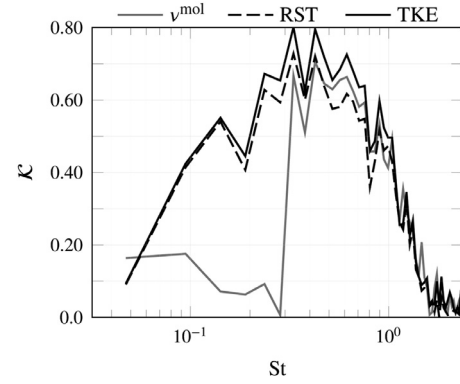


Fig. A.18. Alignment coefficient.

where  $\epsilon$  is a small number. The third approach (Turbulent-Kinetic-Energy (TKE)-model) is based on the mixing length model originally proposed by Prandtl (1925, [74]), relating the eddy-viscosity to a characteristic length  $l_m$  and a velocity  $u^*$

$$\nu_t^{\text{TKE}} = \beta l_m u^*, \quad (\text{A.2})$$

where the scaling constant  $\beta$  is set to 0.05. While an appropriate measure for the characteristic velocity is given by the turbulent kinetic energy  $k = 0.5(\overline{u_x'^2} + \overline{u_r'^2} + \overline{u_\theta'^2})$  with  $u^* = k^{0.5}(\mathbf{x})$  (Kolmogorov, 1942; Prandtl, 1945 [74]), the characteristic length is modeled as a function of the streamwise position

$$l_m(x) = \frac{\overline{u_{x,\text{cl}}}(x)}{\max |\partial_r \overline{u_x}(x)|}, \quad (\text{A.3})$$

where the  $\overline{u_{x,\text{cl}}}(x)$  is the mean flow velocity at the centerline.

Figure A.17 illustrates the turbulence-characteristic quantities involved in the respective models as well as the resulting eddy-viscosity fields. The viscosity from the RST-model shows a local maximum at approximately  $(x, r) = (5, 0.5)D$ , while the eddy-viscosity from the TKE model moderately grows to a streamwise maximum position of  $x = 45D$  (not shown here). In contrast to the TKE-model, the RST-model predicts a distinct eddy-viscosity within the potential core due to very small mean strain rates (Fig. A.17c) and non-vanishing Reynolds stresses (Fig. A.17a).

The agreement between the modes of RA and SPOD is measured quantitatively by means of the alignment coefficient in Eq. (18), which is illustrated for all three models in Fig. A.18 for the non-reacting configuration. The bad performance of the  $\nu^{\text{mol}}$ , especially at low frequencies, emphasizes the necessity for accounting for the turbulent-stochastic interaction via a turbulent eddy-diffusivity. Finally, the TKE model was chosen as eddy viscosity model, since it overall leads to a slightly better agreement of the RA results with the empirical data.

## References

- [1] N. Docquier, S. Candel, Combustion control and sensors: a review, *Prog. Energy Combust. Sci.* 28 (2) (2002) 107–150.
- [2] S. Candel, D. Durox, T. Schuller, N. Darabiha, L. Hakim, T. Schmitt, Advances in combustion and propulsion applications, *Eur. J. Mech. B Fluid* 40 (2013) 87–106.
- [3] T. Liewuven, Modeling premixed combustion-acoustic wave interactions: a review, *J. Propul. Power* 19 (5) (2003) 765–781.
- [4] S. Candel, D. Durox, T. Schuller, Flame interactions as a source of noise and combustion instabilities, 10th AIAA/CEAS Aeroacoustics Conference (2004), pp. 2004–2928.
- [5] S. Candel, D. Durox, S. Ducruix, A.L. Birbaud, N. Noiray, T. Schuller, Flame dynamics and combustion noise: progress and challenges, *Int. J. Aeroacoust.* 8 (1) (2009) 1–56.
- [6] A.P. Dowling, Y. Mahmoudi, Combustion noise, *Proc. Combust. Inst.* 35 (1) (2015) 65–100.
- [7] L.N. Trefethen, A.E. Trefethen, S.C. Reddy, T.A. Driscoll, Hydrodynamic stability without eigenvalues, *Science* 261 (5121) (1993) 578–584.
- [8] B.F. Farrell, P.J. Ioannou, Stochastic forcing of the linearized Navier-Stokes equations, *Phys. Fluids A* 5 (11) (1992) 2600–2609.
- [9] S.C. Reddy, D.S. Henningson, Energy growth in viscous channel flows, *J. Fluid Mech.* 252 (1993) 209–238.
- [10] S.C. Reddy, P.J. Schmid, D.S. Henningson, Pseudospectra of the Orr-Sommerfeld operator, *SIAM J. Appl. Math.* 53 (1) (1993) 15–47.
- [11] Y. Hwang, C. Cossu, Amplification of coherent streaks in the turbulent Couette flow: an input-output analysis at low Reynolds number, *J. Fluid Mech.* 643 (1993) 333–348.
- [12] B. McKeon, A. Sharma, A critical-layer framework for turbulent pipe flow, *J. Fluid Mech.* 658 (2010) 336–382.
- [13] P. Morra, O. Semeraro, D.S. Henningson, C. Cossu, On the relevance of Reynolds stresses in resolvent analyses of turbulent wall-bounded flows, *J. Fluid Mech.* 867 (2019) 969–984.
- [14] L. Abreu, A. Cavalieri, P. Schlatter, R. Vinuesa, D. Henningson, Resolvent modelling of near-wall coherent structures in turbulent channel flow, *Int. J. Heat Fluid Flow* 85 (2020) 108662.
- [15] D. Sipp, O. Marquet, Characterization of noise amplifiers with global singular modes: the case of the leading-edge flat-plate boundary layer, *Theor. Comput. Fluid Dyn.* 27 (5) (2013) 617–635.
- [16] A. Monokrousos, E. Åkervik, L. Brandt, D.S. Henningson, Global three-dimensional optimal disturbances in the Blasius boundary-layer flow using time-steppers, *J. Fluid Mech.* 650 (2010) 181–214.
- [17] C. Cossu, G. Pujals, S. Depardon, Optimal transient growth and very large-scale structures in turbulent boundary layers, *J. Fluid Mech.* 619 (2009) 79–94.
- [18] L.I. Abreu, A.V. Cavalieri, P. Schlatter, R. Vinuesa, D. Henningson, Wavepackets in turbulent flow over a NACA 4412 airfoil, 31st Congress of the International Council of the Aeronautical Sciences, ICAS 2018, 2018.
- [19] X. Garnaud, L. Lesshafft, P.J. Schmid, P. Huerre, The preferred mode of incompressible jets: linear frequency response analysis, *J. Fluid Mech.* 716 (2013) 189–202.
- [20] S. Beneddine, R. Yegavian, D. Sipp, B. Leclaire, Unsteady flow dynamics reconstruction from mean flow and point sensors: an experimental study, *J. Fluid Mech.* 824 (2017) 174–201.
- [21] O.T. Schmidt, A. Towne, G. Rigas, T. Colonius, G.A. Br, Spectral analysis of jet turbulence, *J. Fluid Mech.* 855 (1971) (2018) 953–982.
- [22] J. Jeun, J.W. Nichols, M.R. Jovanović, Input-output analysis of high-speed axisymmetric isothermal jet noise, *Phys. Fluids* 28 (4) (2016) 047101.
- [23] E.M. Pickering, A. Towne, P. Jordan, T. Colonius, Resolvent-based jet noise models: a projection approach, AIAA Scitech 2020 Forum (2020), p. 2020-0999.
- [24] T.L. Kaiser, L. Lesshafft, K. Oberleithner, Prediction of the flow response of a turbulent flame to acoustic perturbations based on mean flow resolvent analysis, *J. Eng. Gas Turbines Power* 141 (11) (2019).
- [25] H. Nawroth, C.O. Paschereit, F. Zhang, P. Habisreuther, H. Bockhorn, Flow investigation and acoustic measurements of an unconfined turbulent premixed jet flame, 43rd Fluid Dynamics Conference (2013), pp. 2013–2459.
- [26] F. Zhang, P. Habisreuther, H. Bockhorn, H. Nawroth, C.O. Paschereit, On prediction of combustion generated noise with the turbulent heat release rate, *Acta Acust. United Acust.* 99 (6) (2013) 940–951.
- [27] J. Lumley, The structure of inhomogeneous turbulent flows, *Atmos. Turbul. Radio Propag.* (ed. A. M. Yaglom & V. I. Tatarski) (1967) 166–178.
- [28] J.L. Lumley, Stochastic tools in turbulence, Academic Press, New York, 1970.
- [29] A. Towne, O.T. Schmidt, T. Colonius, Spectral proper orthogonal decomposition and its relationship to dynamic mode decomposition and resolvent analysis, *J. Fluid Mech.* 847 (2018) 821–867.
- [30] E. Pickering, G. Rigas, P.A. Nogueira, A.V. Cavalieri, O.T. Schmidt, T. Colonius, Lift-up, Kelvin-Helmholtz and Orr mechanisms in turbulent jets, *J. Fluid Mech.* 896 (2020).
- [31] T. Shoji, Y. Iwasaki, K. Kato, S. Yoshida, S. Tachibana, T. Yokomori, Effects of flame structures on direct combustion noise produced by lean-Premixed H<sub>2</sub>/air low-swirl jet flames, AIAA Scitech 2020 Forum (2020), p. 2020-0918.
- [32] F. Nicoud, L. Benoit, C. Sensiau, T. Poinsot, Acoustic modes in combustors with complex impedances and multidimensional active modes, *AIAA J.* 45 (2) (2007) 426–441.
- [33] S. Bragg, Combustion noise, *J. Inst. Fuel* 36 (1) (1963) 12–16.
- [34] F. Zhang, T. Zirwes, P. Habisreuther, H. Bockhorn, D. Trimis, H. Nawroth, C.O. Paschereit, Impact of combustion modeling on the spectral response of heat release in les, *Combust. Sci. Technol.* 191 (9) (2019) 1520–1540.
- [35] F. Zhang, P. Habisreuther, M. Hettel, H. Bockhorn, Modeling of a premixed swirl-stabilized flame using a turbulent flame speed closure model in les, *Flow Turbul. Combust.* 82 (2009) 537–551.
- [36] F. Zhang, P. Habisreuther, H. Bockhorn, H. Nawroth, C.O. Paschereit, Combustion generated noise: an environment related issue for future combustion systems, *Energy Technol.* 5 (7) (2017) 1045–1054.
- [37] F. Zhang, T. Zirwes, P. Habisreuther, N. Zarzalis, H. Bockhorn, D. Trimis, Numerical simulations of turbulent flame propagation in a fan-stirred combustion bomb and bunsen-burner at elevated pressure, *Flow Turbul. Combust.* 106 (2020) 925–944.
- [38] OpenFOAM, The open source CFD toolbox, 2014.
- [39] J. Fröhlich, Large Eddy simulation turbulenter Strömungen, Teubner Verlag, 2006.
- [40] D. Goodwin, H. Moffat, R. Speth, Cantera: an object-oriented software toolkit for chemical kinetics, thermodynamics, and transport processes. version 2.3.0b, 2017.
- [41] G.P. Smith, D. Golden, M. Frenklach, N. Moriarty, B. Eiteneer, M. Goldenberg, C. Bowman, R. Hanson, S. Song, W. Gardiner Jr, et al., Grimech 3.0 reaction mechanism, Sandia National Laboratory, 2000.
- [42] M. Klein, A. Sadiki, J. Janicka, A digital filter based generation of inflow data for spatially developing direct numerical or large eddy simulations, *J. Comput. Phys.* 286 (2003) 652–665.
- [43] T. Poinsot, S.K. Lele, Boundary conditions for direct simulation of compressible viscous flows, *J. Comput. Phys.* 101 (1992) 104–129.
- [44] T. Poinsot, D. Veynante, Theoretical and numerical combustion, 3, R.T. Edwards Inc., 2012.
- [45] W.C. Reynolds, A.K. Hussain, The mechanics of an organized wave in turbulent shear flow. Part 3. Theoretical models and comparisons with experiments, *J. Fluid Mech.* 54 (2) (1972) 263–288.
- [46] K. Manoharan, S. Hemchandra, Absolute/convective instability transition in a backward facing step combustor: fundamental mechanism and influence of density gradient, *J. Eng. Gas Turbines Power* 137 (2) (2014) 021501.
- [47] F. Viola, G.V. Iungo, S. Camarri, F. Porté-Agel, F. Gallaire, Prediction of the hub vortex instability in a wind turbine wake: stability analysis with eddy-viscosity models calibrated on wind tunnel data, *J. Fluid Mech.* 750 (2014) 499–526.
- [48] K. Oberleithner, M. Stöhr, S.H. Im, C.M. Arndt, A.M. Steinberg, Formation and flame-induced suppression of the precessing vortex core in a swirl combustor: experiments and linear stability analysis, *Combust. Flame* 162 (8) (2015) 3100–3114.
- [49] L. Rukes, C.O. Paschereit, K. Oberleithner, An assessment of turbulence models for linear hydrodynamic stability analysis of strongly swirling jets, *Eur. J. Mech. B Fluid* 59 (2016) 205–218.
- [50] P. Paredes, S. Terhaar, K. Oberleithner, V. Theofilis, C.O. Paschereit, Global and local hydrodynamic stability analysis as a tool for combustor dynamics modeling, *J. Eng. Gas Turbines Power* 138 (2) (2016) 021504.
- [51] M. Vanierschot, J.S. Müller, M. Sieber, M. Percin, B.W. van Oudheusden, K. Oberleithner, Single- and double-helix vortex breakdown as two dominant global modes in turbulent swirling jet flow, *J. Fluid Mech.* 883 (2020) A31.
- [52] J.C. del Álamo, J. Jiménez, Linear energy amplification in turbulent channels, *J. Fluid Mech.* 559 (2006) 205–213.
- [53] T.L. Kaiser, K. Oberleithner, A global linearized framework for modelling shear dispersion and turbulent diffusion of passive scalar fluctuations, *J. Fluid Mech.* (2021) A111. (in press)
- [54] P. Kuhn, T. Kaiser, J. Soria, K. Oberleithner, Spectral decomposition of the turbulent self-similar jet and recomposition using linear dynamics, 11th International Symposium on Turbulence and Shear Flow Phenomena, 2019.
- [55] E.M. Pickering, G. Rigas, D. Sipp, O.T. Schmidt, T. Colonius, Eddy viscosity for resolvent-based jet noise models, 25th AIAA/CEAS Aeroacoustics Conference, Paper 2019–2454 (2019).
- [56] R.G. Rehm, H.R. Baum, Equations of motion for thermally driven, buoyant flows, *J. Res. Natl. Bur. Stand.* 83 (3) (1978) 297–308.
- [57] J.-M. Chomaz, Global instabilities in spatially developing flows: non-normality and nonlinearity, *Annu. Rev. Fluid Mech.* 2 (2004) 357–392.
- [58] O. Tammisola, M.P. Juniper, Coherent structures in a swirl injector at  $re = 4800$  by nonlinear simulations and linear global modes, *J. Fluid Mech.* 792 (2016) 620–657.
- [59] F. Gianetti, P. Luchini, Structural sensitivity of the first instability of the cylinder wake, *J. Fluid Mech.* 581 (2007) 167–197.
- [60] M.S. Alnæs, J. Blechta, J. Hake, A. Johansson, B. Kehllet, A. Logg, C. Richardson,

- J. Ring, M.E. Rognes, G.N. Wells, The fenics project version 1.5, *Arch. Numer. Softw.* 3 (100) (2015) 9–23.
- [61] R.B. Lehoucq, D.C. Sorensen, C. Yang, *ARPACK users guide: solution of large scale eigenvalue problems by implicitly restarted Arnoldi methods*, Software, environments, tools, SIAM, 1997.
- [62] M.R. Khorrami, M.R. Malik, R.L. Ash, Application of spectral collocation techniques to the stability of swirling flows, *J. Comput. Phys.* 81 (1) (1989) 206–229.
- [63] L. Lesshafft, Artificial eigenmodes in truncated flow domains, *Theor. Comput. Fluid Dyn.* 32 (2018) 245–262.
- [64] T.C. Lieuwen, *Unsteady combustor physics*, Cambridge University Press, 2012.
- [65] H. Wang, C. Law, T. Lieuwen, Linear response of stretch-affected premixed flames to flow oscillations, *Combust. Flame* 156 (2009) 889–895.
- [66] P. Preetham, S.K. Thumuluru, H. Santosh, T. Lieuwen, Linear response of laminar premixed flames to flow oscillations: unsteady stretch effects, *J. Propul. Power* 26 (2010) 524–532.
- [67] S. Hemchandra, N. Peters, T. Lieuwen, Heat release response of acoustically forced turbulent premixed flames—role of kinematic restoration, *Proc. Combust. Inst.* 33 (2011) 1609–1617.
- [68] T. Schuller, D. Durox, S. Candel, Self-induced combustion oscillations of laminar premixed flames stabilized on annular burners, *Combust. Flame* 135 (2003) 525–537.
- [69] K. Oberleithner, S. Schimek, C.O. Paschereit, Shear flow instabilities in swirl-stabilized combustors and their impact on the amplitude dependent flame response: a linear stability analysis, *Combust. Flame* 162 (2015) 86–99, doi:10.1016/j.combustflame.2014.07.012. URL: <https://www.sciencedirect.com/science/article/pii/S0010218014002077>
- [70] A. Albayrak, D.A. Bezin, W. Polifke, Response of a swirl flame to inertial waves, *Int. J. Spray Combust. Dyn.* 10 (2018) 277–286.
- [71] M. Merk, W. Polifke, R. Gaudron, M. Gatti, C. Mirat, T. Schuller, Measurement and simulation of combustion noise and dynamics of a confined swirl flame, *AIAA J.* 56 (2018) 1930–1942, doi:10.2514/1.j056502.
- [72] T.L. Kaiser, K. Oberleithner, L. Selle, T. Poinot, Examining the effect of geometry changes in industrial fuel injection systems on hydrodynamic structures with global linear stability analysis, *J. Eng. Gas Turbines Power* 142 (1) (2020).
- [73] O. Semeraro, L. Lesshafft, V. Jaunet, P. Jordan, Modeling of coherent structures in a turbulent jet as global linear instability wavepackets : theory and experiment, *Int. J. Heat Fluid Flow* 62 (2016) 24–32.
- [74] S.B. Pope, *Turbulent flows*, Cambridge University Press, 2000.